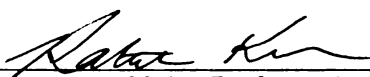This is to certify that the
thesis entitled

DESIGN VARIATIONS AND IMPROVEMENTS OF
PERSPIRABLE SKIN

presented by

JIN ZHANG TAM

has been accepted towards fulfillment
of the requirements for the

____M.S.____ degree in ____Mechanical Engineering____

_____
Major Professor's Signature

_____8/2/2010_____
Date

PLACE IN RETURN BOX to remove this checkout from your record.
TO AVOID FINES return on or before date due.
MAY BE RECALLED with earlier due date if requested.

DATE DUE	DATE DUE	DATE DUE
AUG 3 _ 2012		

DESIGN VARIATIONS AND IMPROVEMENTS OF PERSPIRABLE SKIN

By

JIN ZHANG TAM

A THESIS

Submitted to
Michigan State University
in partial fulfillment of the requirements
for the degree of

MASTER OF SCIENCE

Mechanical Engineering

2010

ABSTRACT

DESIGN VARIATIONS AND IMPROVEMENTS OF PERSPIRABLE SKIN

By

JIN ZHANG TAM

An autonomous deforming and reusable self-cooling thermal protection system (TPS) was designed and modified for surfaces operating in extreme temperatures such as the surface of the space shuttle. This newly designed structure, called 'Perspirable Skin,' contains cores and deformable rings that are fitted into Reinforced Carbon-Carbon (RCC) composite skin. The cores and deformable rings are made of a composition of pure ZrW_2O_8 (zirconium tungstate) and ZrO_2 (zirconia), which forms a Functionally Graded Material (FGM). The choice of ZrW_2O_8 is due to its highly negative coefficient of thermal expansion (CTE) in a wide range of temperatures. When the temperature increases, the core would shrink while the deformable ring would have an out-of-plane deformation to create a large gap. The compressed coolant gas onboard is blown through this gap onto the surface. The coolant gas is expected to mix with the surface air to eliminate the frictional heating. The geometry and stacking sequence of the cores as well as the deformable rings were designed by Finite Element Method (FEM). Possibilities of other negative coefficient of thermal expansion materials were discussed and explored.

To my dear parents and Jomay.

ACKNOWLEDGEMENTS

I would like to express my gratitude to my advisor Dr. Patrick Kwon for giving me the opportunity to work on this Perspirable Skin project and for his invaluable supervision and support throughout the course as a Master's student at Michigan State University. I would also like to thank Dr. Dahsin Liu and Dr. Alfred Loos for being on my thesis committee.

I am delighted to have such a valuable opportunity to work with a group of very knowledgeable colleagues on this project. I would like to give thanks to Li Sun and Basak Oguz who have been the pioneers to explore and have laid a good foundation for the research work. I would also like to thank Mingang Wang, Mayeul de La Tour du Pin and Matt Lempke for their assistance in conducting lab experiments and contributions to the research work.

Finally, I would like to thank my family and friends for their countless support and encouragement. They have helped me through difficult times and they are always with me through the ups and downs. Without them, I would not have been able to finish this task. Thank you very much!

TABLE OF CONTENTS

LIST OF TABLES

LIST OF FIGURES

INTRODUCTION

When a space shuttle is returning to earth from its mission in space, the temperatures on different regions, such as the nose and the leading edges of the wings of the outer surfaces of the space shuttle would be extremely high. These surface temperatures could reach as high as 1,650 °C [1], occurring at 20 minutes before landing [1]. These high temperatures are caused by the surface friction of the shuttle and atmospheric gases when the space shuttle is trying to slow down to the landing speed from a velocity exceeding 25,000 mph [1, 2].

The space shuttle orbiter is built mainly with 2024-T6 aluminum and graphite-epoxy [3]; both materials can only withstand a temperature up to 175 °C. A Thermal Protection System (TPS) is a crucial component to the shuttle because it prevents heat from transferring to the shuttle structure [2, 3], which eliminates the possibility of the structure degradation and thus protects the astronauts on board.

The goal of this "Perspirable Skin" project, which is supported by Air Force Office of Scientific Research (AFOSR), is carried out in an effort to design and fabricate the prototype of an intelligent and automatic self-cooling system to the TPS that are exposed to the highest temperatures during the crucial stage of the re-entry. This project is divided into several stages. At the beginning stage, exploration of suitable materials and a working design have been achieved. The motivation of

this thesis is focused on the second stage of the project, which is to modify and experiment with other possible designs to create an out-of-plane gap deformation. The objective is to achieve a larger gap opening through the incorporation of an additional deformable ring to the current design.

CHAPTER 1

THE SPACE SHUTTLE – IN-DEPTH REVIEW

THERMAL PROTECTION SYSTEM

The orbiter operates at extreme temperatures as low as -157 °C while in outer space; during re-entry the orbiter is oriented with the nose angled up about 40 degrees from the horizontal. This stage would last for about 25 minutes. In between 45 and 80 km above the ground, the space shuttle must endure tremendous heating, reaching a temperature as high as 1,650 °C [2, 3]. Other than these two extreme conditions, the orbiter has to withstand local heating from the engines, motors, and thrusters on board. Due to the wide variety of temperatures that the space shuttle experiences in its mission, the TPS is composed of different materials that have been carefully chosen and tested.

In an earlier NASA report, which dated back to 1989, it was revealed that the surface temperatures distribution of a space shuttle as shown in Figure 1, reaches a maximum temperature of 1,440 °C [3]. A more recent investigation confirmed that the maximum temperature the space shuttle would experience could reach 1,650°C [2]. Therefore, the materials that made up the TPS have different material properties in order to handle these complex and extreme thermal loading conditions.
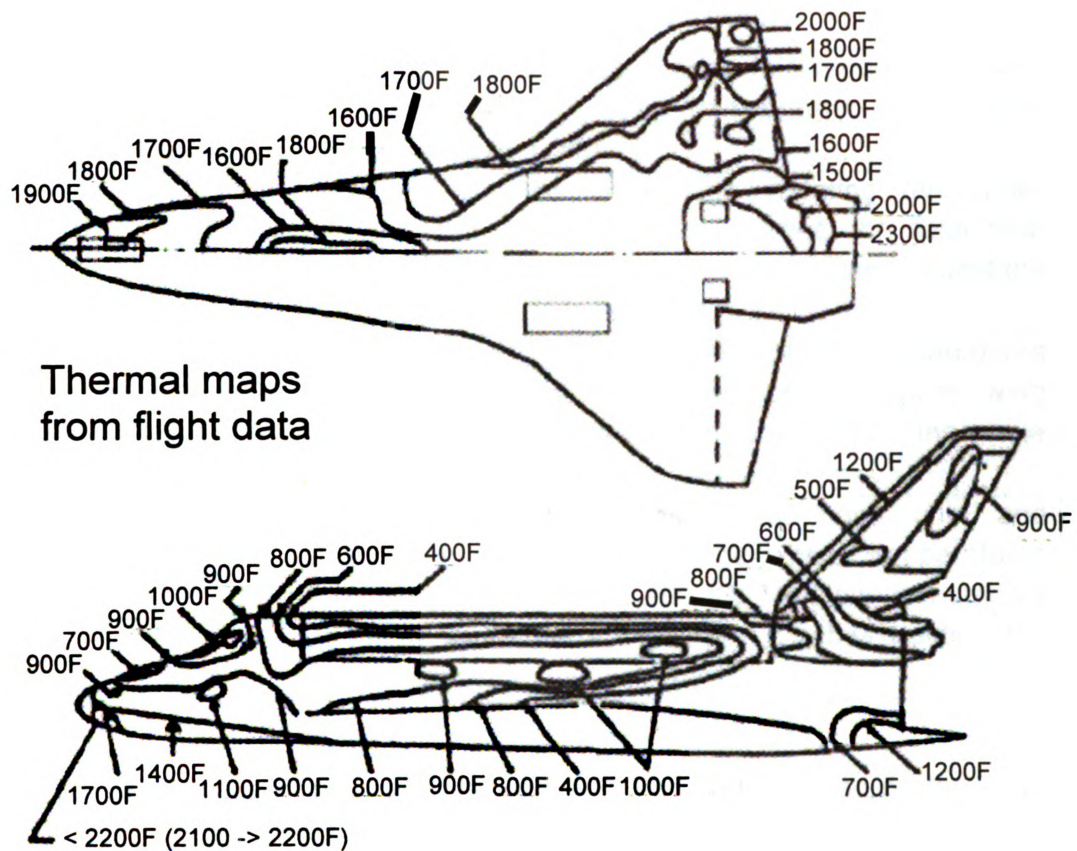
Figure 1. Surface temperature distribution of the space shuttle [11]

The TPS has been improved over the years, current TPS uses 3 types of tiles, 2 types of insulation blankets, and the RCC as shown in Figure 2. There are about 24,300 tiles and 2,300 flexible insulation blankets covering the outer surface of the orbiter [2]. These tiles and blankets cover different parts of the orbiter depending on their properties and the respective heating conditions on different locations of the orbiter. Each of these tiles or blankets has different thermal properties and can withstand different temperatures as listed in Table 1 below.

Table 1. Usage of different tiles and blankets [2]

Category	Description
High-Temperature Reusable Surface Insulation (HRSI) Tiles	They have a black coating to evacuate the heat during re-entry. They can protect the covered areas up to 1,260 °C.
Low-Temperature Reusable Surface Insulation (LRSI) Tiles	They are the white tiles covering the upper surfaces of the orbiter and reflect the solar heat gain from the sun. They can withstand temperatures up to 650 °C.
Felt Reusable Surface Insulation (FRSI) Blankets	They cover the upper section of the payload doors and the inboard sections of the upper wing surfaces. They also cover about 25% of the whole vehicle up to 370°C.
Reinforced Carbon-Carbon (RCC)	They cover the areas on the nose, chin, and leading edge of the wings where temperatures can be as high as 1,260 °C. They can withstand a high temperature of 1,770 °C while holding the structure.

There are other types of tiles and blankets that also can be used on the space shuttle. Fibrous Refractory Composite Insulation (FRCI) tiles can be used to replace HRSI tiles in some areas. Another type of blanket, Advanced Flexible Reusable Surface Insulation (AFRSI), can replace most of the LRSI tiles in order to achieve the flight requirements more effectively [2].
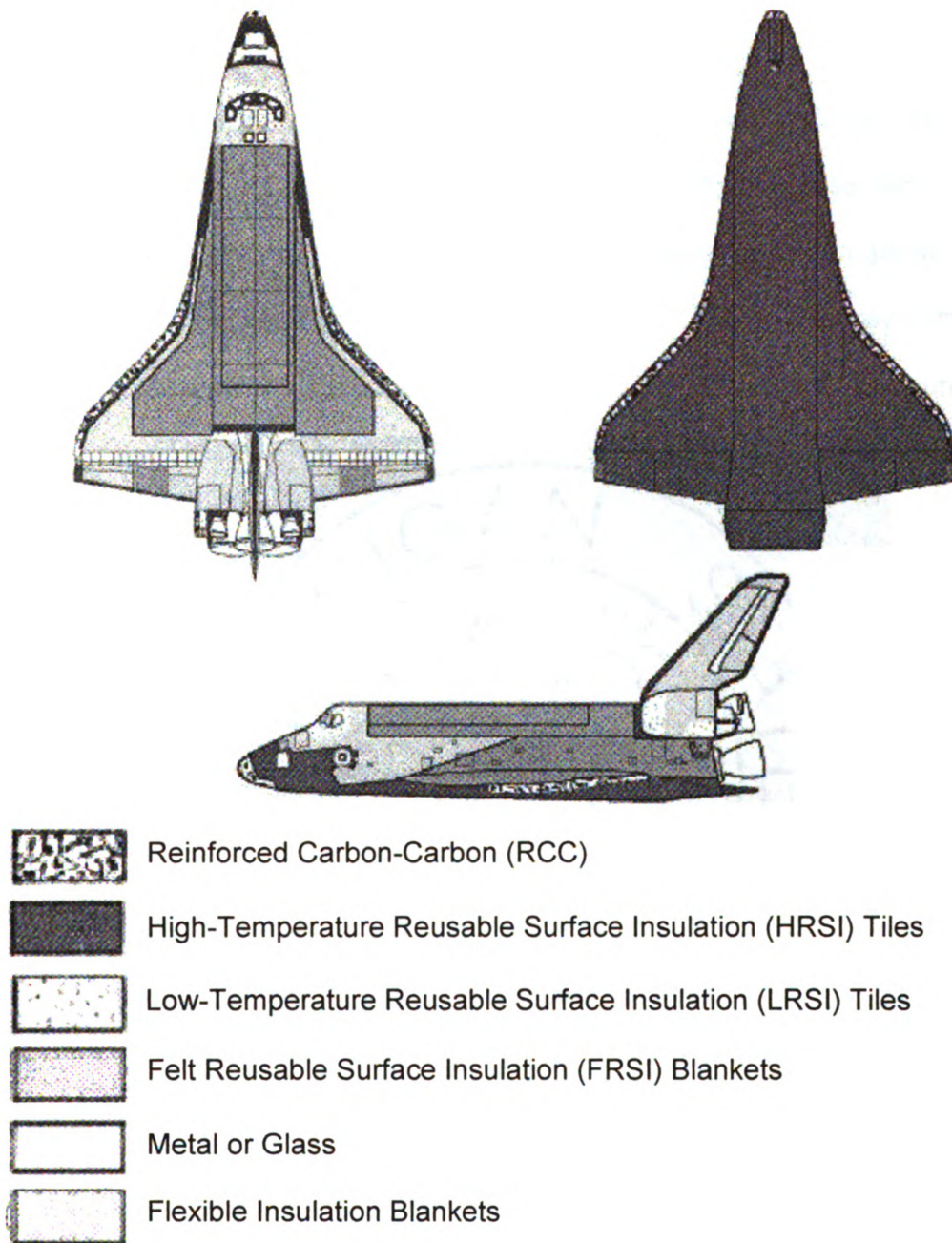
Figure 2. TPS tile distribution on the space shuttle [2]

Reinforced Carbon-Carbon (RCC)

High-Temperature Reusable Surface Insulation (HRSI) Tiles

Low-Temperature Reusable Surface Insulation (LRSI) Tiles

Felt Reusable Surface Insulation (FRSI) Blankets

Metal or Glass

Flexible Insulation Blankets

REINFORCED CARBON-CARBON (RCC) PANEL

Some of the hottest areas on the surface of the space shuttle during the re-entry are the nose cap; the chin, which is directly beneath the nose cap; and the leading edge of the wings [4, 5]. Temperatures in these areas can get as high as nearly 1,700 °C. These areas are covered by RCC, which is a gray composite, along with Inconel foil insulators and quartz blankets [6] as shown in Figure 3.
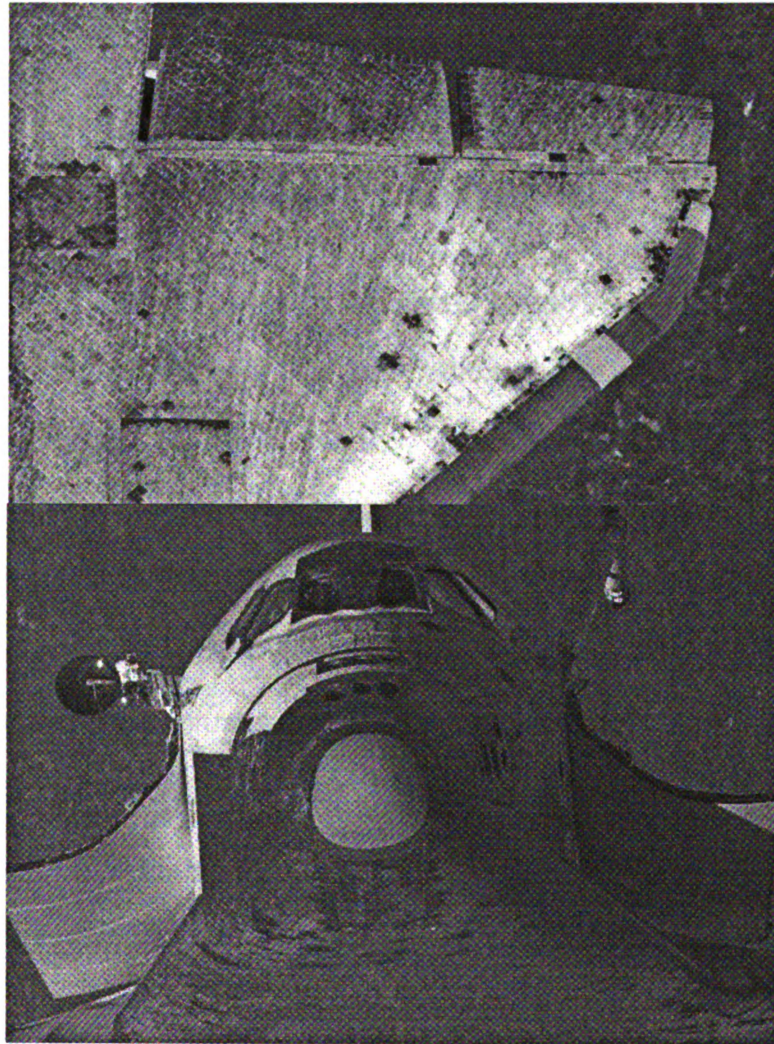
Figure 3. RCC panels on leading edge of wings, nose, and chin (NASA)

The leading edge of the wings have 22 RCC panels installed and they are approximately 6.3 mm thick; on the nose cap the thicknesses of these panels are between 6.3 mm and 12.7 mm as shown in Figure 4 below.
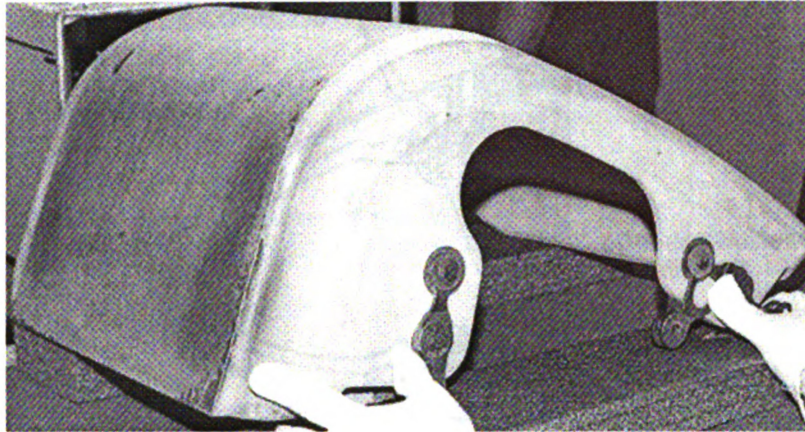
Figure 4. RCC wing panel [8]

These panels are manufactured by Lockheed-Martin's Missile and Fire Control Facilities. The public has very little information on the material properties and performance on the RCC panels as they are classified materials. RCC panels have relatively high thermal conductivity of approximately 70 W/m/K. As a result, additional insulation blankets such as the Cerachrome are needed to stop the heat transfer behind the RCC panels. There are also other alloys and metals such Al 2024 and titanium used to support the structure [7, 8].
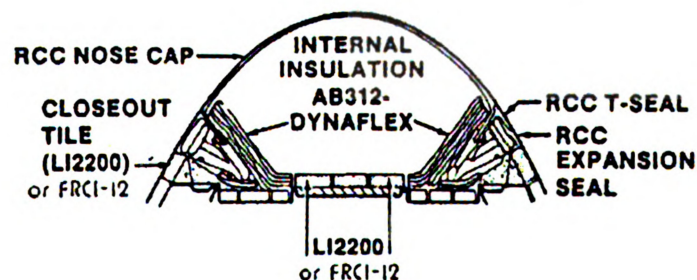
Figure 5. RCC on the nose [3]
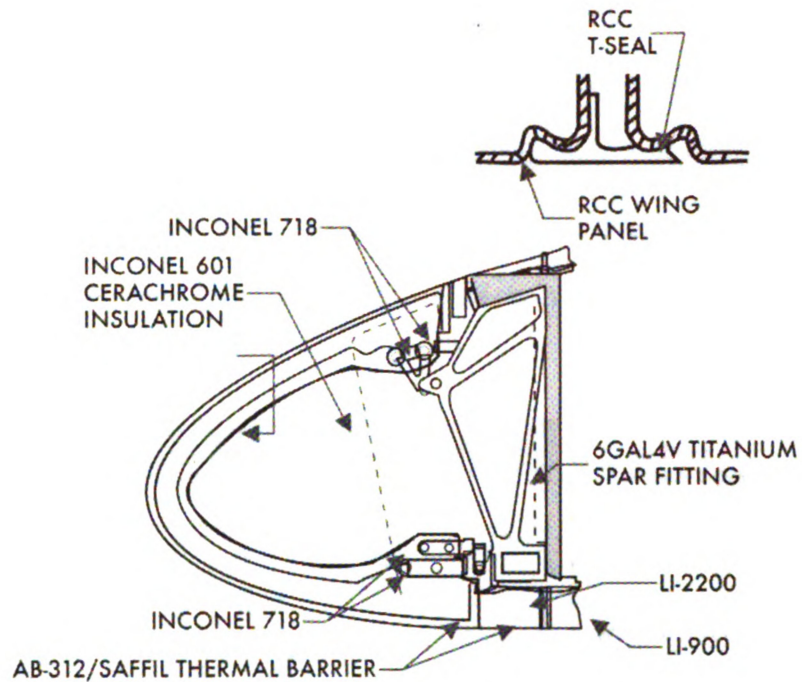
Figure 6. RCC on the wing [10]

In Figure 6, the Inconel 718 and Inconel 601 foils are used to stop the heat transfer from the outermost surfaces into the structural support and interior of the space shuttle. Table 2 gives the details of their respective operating temperatures.

Table 2. Operating conditions of the materials underneath the RCC panels

Alloy	Usage	Maximum service temperature (°C)	Approximate melting point (°C)
IN 718	Clevis, spanner beam	980	1,370
IN 601	Spar insulation foil	1,090	1,370
Al 2024	Wing spar	N/A	650

Carbon/carbon composites without any treatment and coating begin to oxidize at around 500 °C [9]. Oxidation of the carbon/carbon composites greatly jeopardize the safety and integrity of the space shuttle. In order to protect the carbon/carbon

composites, a RCC panel is coated with a layer of silicon carbide (SiC) and then it is vacuum infiltrated with a phenolic resin to fill the voids in between. Due to the different coefficients of thermal expansion of the two materials, an additional sealant of sodium silicate glass is coated on top to prevent crack formation and oxidation [7, 8]. Figure 7 shows the cross section of a RCC panel with the 3 layers of material.
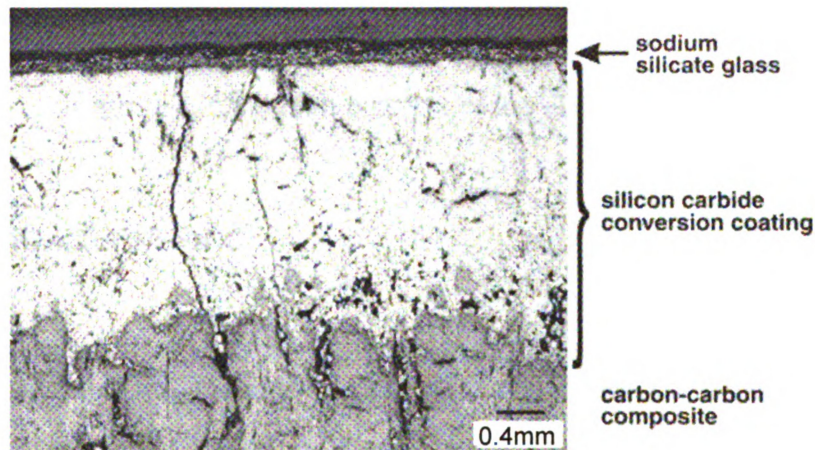
Figure 7. Cross section of RCC [7]

Despite the coating and sealant, oxidation of the RCC cannot be prevented. The degradation of the RCC panel begins when the micro-cracks are formed on the coating as shown in Figure 8. The oxidation process worsens as more and more oxygen penetrates the coating and reacts with the carbon/carbon composite, and finally with intense friction and ablation of the air outside, the coating would be peeled off, exposing the carbon/carbon composites to the atmosphere.

New RCC

Increasing Interfacial Oxidation
With Flight Exposure

SIC Debond

SIC

Carbon

| Craze cracks provide an oxidation path to the silicon carbide to carbon interface | Small amounts of oxygen penetrate the coating and react with the carbon matrix and fibers, resulting in a decrease in strength | Increasing oxidation areas decrease the adherence of the silicon carbide "craze squares" to the substrate | Silicon carbide "craze squares" may become dislodged by external forces (airloads, impact, acoustics, flexure) |

Figure 8. Oxidation process of the RCC panel [10]

OPERATING CONDITIONS

One of the tasks of this thesis is to perform a more in-depth study to understand the actual operating conditions of the space shuttle during a re-entry. In the previous work, the operating conditions were unclear and the thermal loading conditions, temperatures, and many other parameters were estimated. Some of the finite element method simulations were approximations of idealistic assumptions.

After the tragedy of the Columbia space shuttle disintegration on February 1, 2003, NASA conducted a thorough investigation and studies on the re-entry. The report of the Columbia tragedy has provided a lot of simulated results, which have provided a better understanding of the actual conditions during a re-entry. In the computational fluid dynamics (CFD) solution in Figure 9, which simulated

the re-entry of the space shuttle, the vehicle enters the atmosphere with an angle of attack of 39.59 degrees, at an altitude of 69.319 km. The velocity of the space shuttle reached a Mach number of 22.91, which is equivalent to 6.76 km/s.

Flow

| T (K) | 0 | 1300 | 2600 | 3900 | 5200 | 6500 | 7800 | 9100 | 10400 | 11700 | 13000 |
| T (F) | -460 | 1880 | 4220 | 6560 | 8900 | 11240 | 13580 | 15920 | 18260 | 20600 | 22940 |
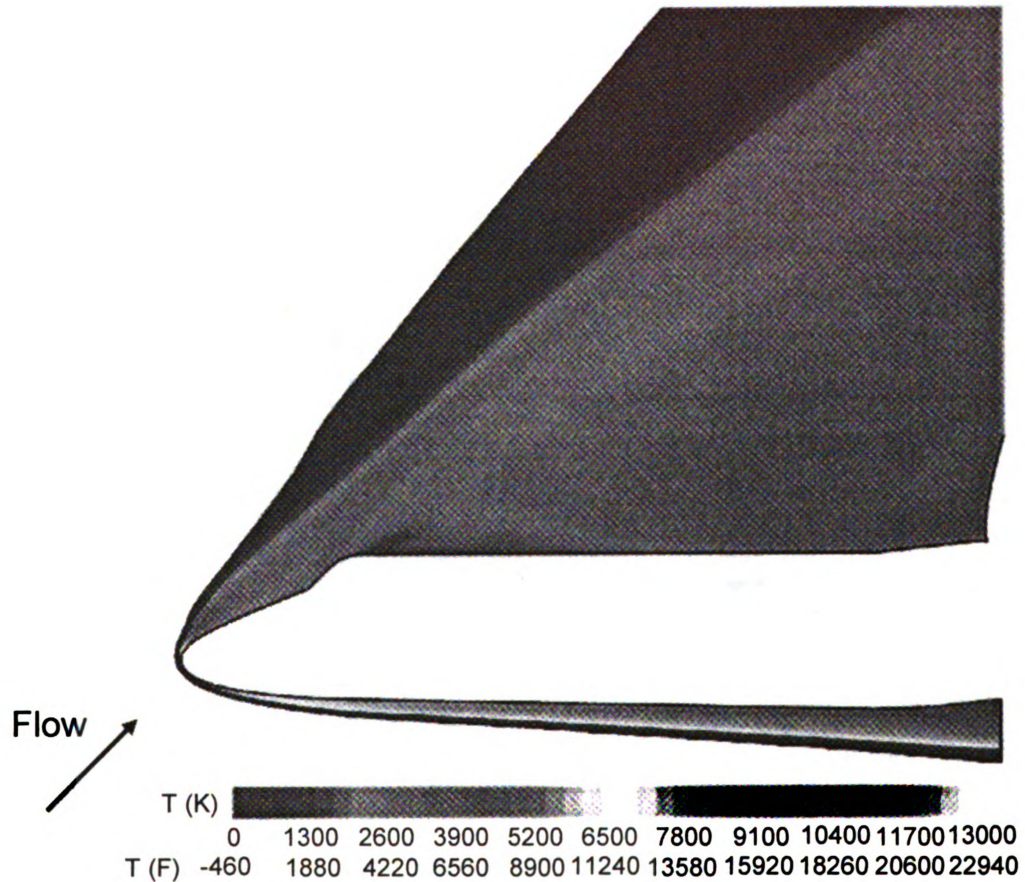
Figure 9. Gas temperatures from the CFD solution [11]

The surrounding gas temperatures in the simulation revealed that gas near the nose and chin of the space shuttle could reach a temperature over 10,000 °C [11]. The high temperature would be caused by the friction between the air and the surface of the space shuttle at great velocity.

The report also simulated the surface temperatures and the surface pressures on the space shuttle in Figure 10 and Figure 11 respectively. Because the space shuttle was entering the atmosphere at approximately 40 degrees to the horizontal, most of the high temperature and pressure regions occur at the belly and the lower surfaces of the wings.

T (K)	T (°F)
1900	2960
1740	2672
1580	2384
1420	2096
1260	1806
1100	1520
940	1232
780	944
620	656
460	368
300	80

T (K)	T (°F)
1900	2960
1740	2672
1580	2384
1420	2096
1260	1806
1100	1520
940	1232
780	944
620	656
460	368
300	80
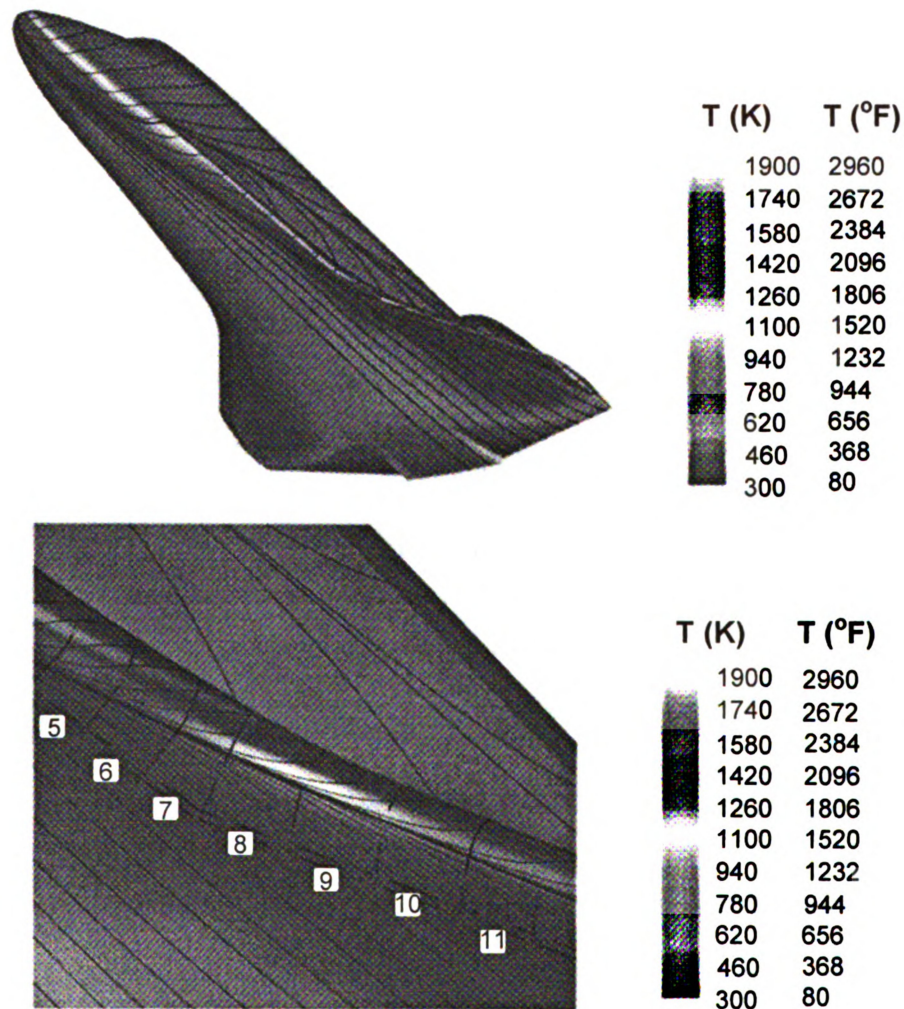
Figure 10. Surface temperatures from CFD solution [11]
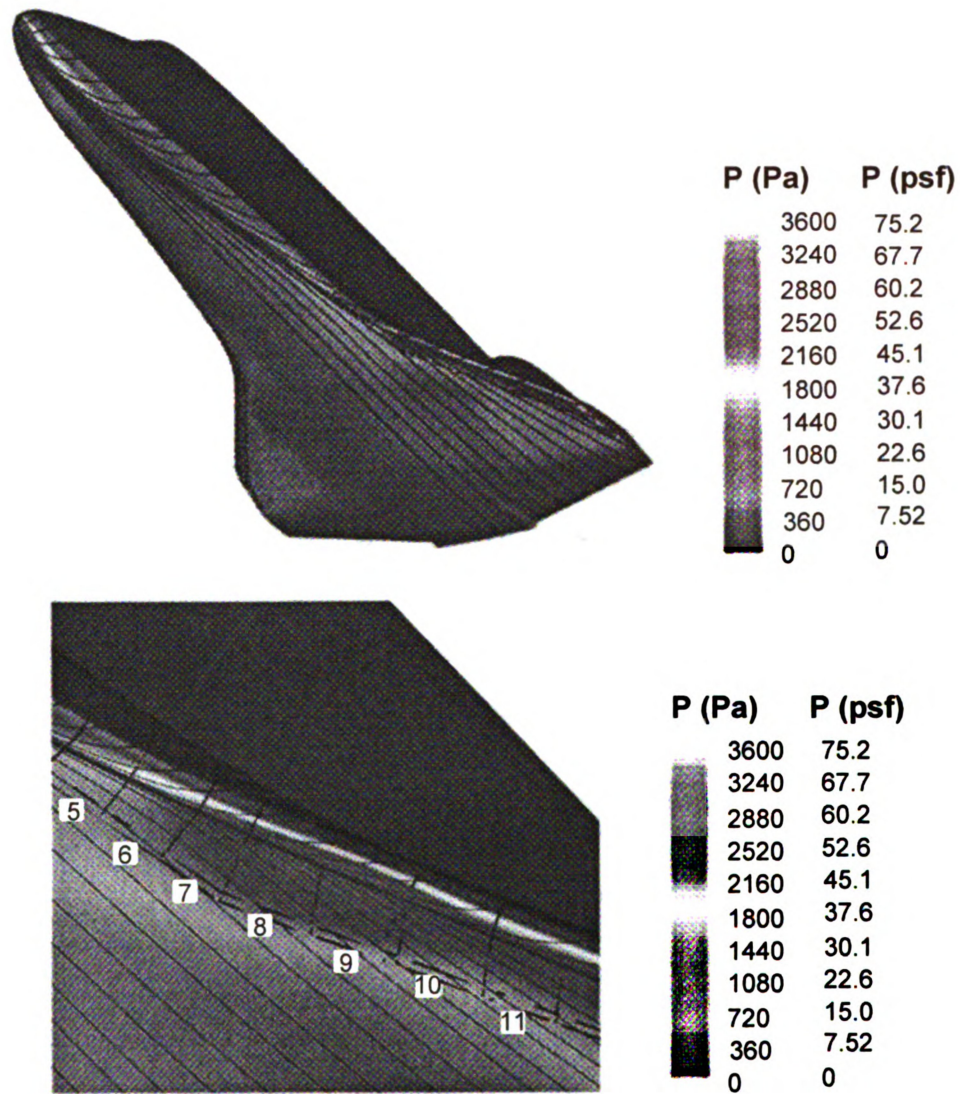
Figure 11. Surface pressures from CFD solution [11]

It can be observed from these two figures that the highest temperatures and pressures locations fall on the nose, chin, and the leading edge of the wings reaching approximately 1630 °C and 3000 Pa. Most of the lower surface of the space shuttle had a temperature over 1000 °C and 1000 Pa.

THERMAL LOADING CONDITIONS

With little understanding of the actual operating conditions during the re-entry of the space shuttle, previous finite element method simulations were based on the assumption that the outside air temperature was a constant at 760 °C. This assumption was based on the fact that ZrW_2O_8 dissociates at a temperature around 800 °C. In order to produce more accurate simulation results that are as close to the actual condition as possible, it is important to study the thermal loading conditions during the re-entry.
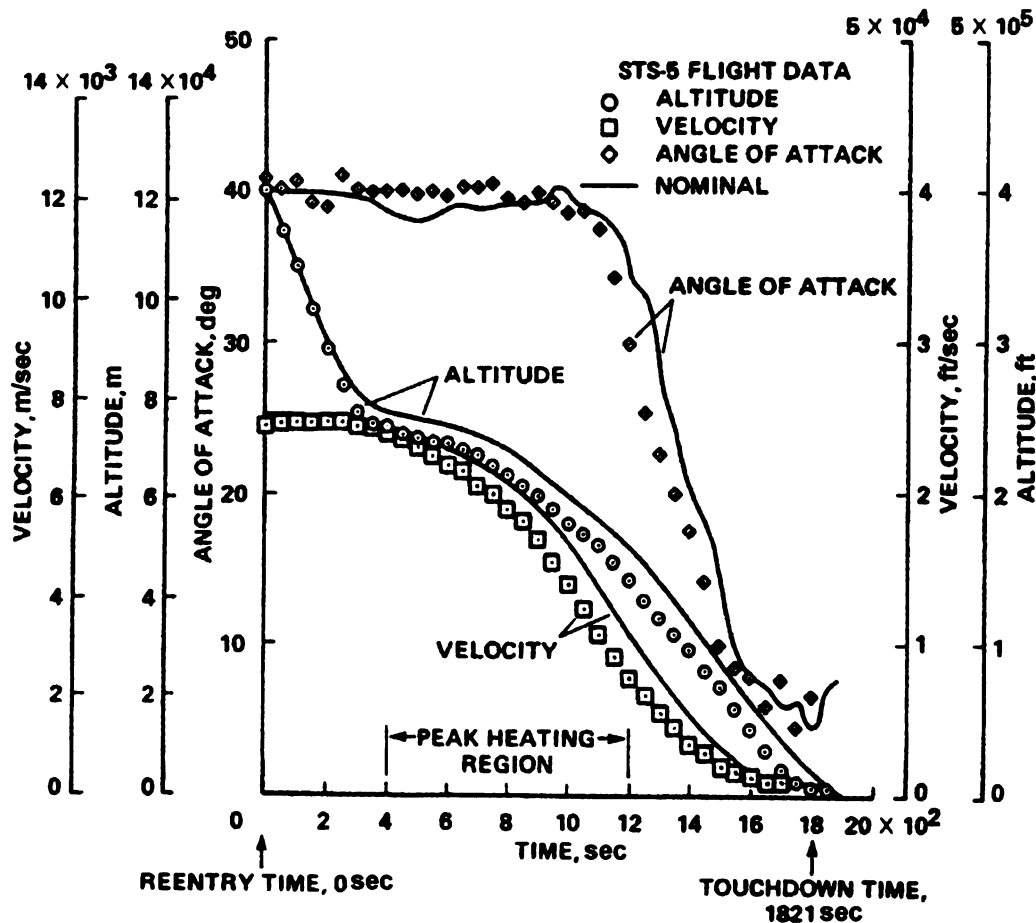
Figure 12. STS-5 mission data of space shuttle Columbia [12]

15

In the data collected from the mission STS-5 with space shuttle Columbia in 1982, as shown in Figure 12, a re-entry process lasts for approximately 1,800 seconds where there are about 800 seconds in which the space shuttle undergoes intense heating. The exact phenomenon that is occurring during the re-entry is too complicated to predict. It can be caused by a combination of the viscous dissipation in the boundary layers, the thermal radiation, and transition to turbulence and instabilities on the curve walls or the strong shock layers and thermo-chemical effects [13].

The re-entry process started at an altitude of 120 km. Between 120 km and 80 km, the density of the air increases as the altitude decreases, but the velocity of the space shuttle remains steady. The peak heating region starts when the space shuttle is between 80 km and 45 km of altitude. Most of the kinetic energy is dissipated into heat, resulting in the velocity of the orbiter being greatly reduced by friction and drag.

To study the thermal loading conditions, there are three hypotheses assumed in order to simplify the problem. Referring to Figure13, the maximum heat flux, which occurs at the peak heating time during the re-entry, is relatively steady. Therefore, one can assume that a steady state is reached between the absorbed heat and the emitted heat during that period of time.
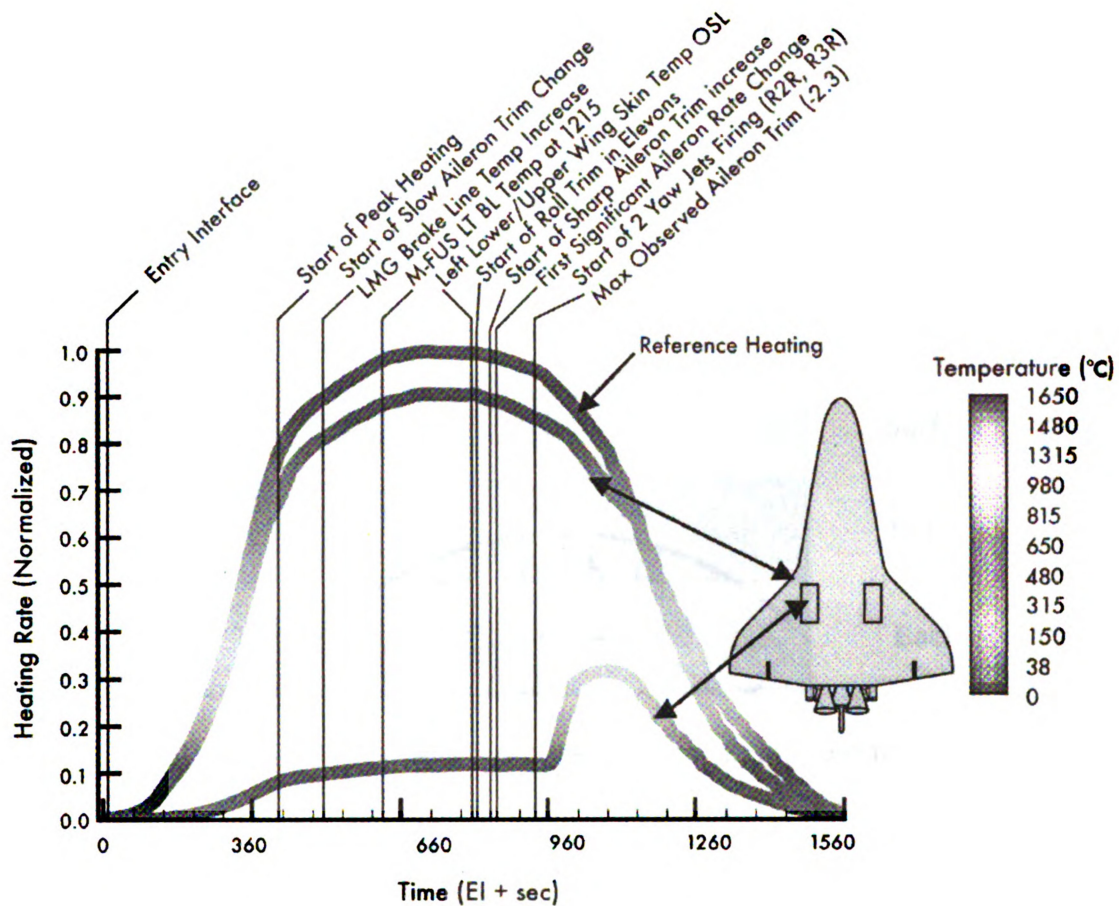
Figure 13. Heating rate profile [10]

According to [13], most of the heat is stopped near the outer surface of the space shuttle. There are layers of insulations behind the RCC layer; therefore, another assumption made in simplifying the problem is to neglect the conductive heat flux that goes into the surface coating in Figure 14.

The last assumption neglects the radiation flux going into the TPS system because as the space shuttle travels at a speed below 8 km/s, the radiation flux from the atmosphere (radiation flux in (1) in Figure 14) is very small compared to the convective heat flux.

17
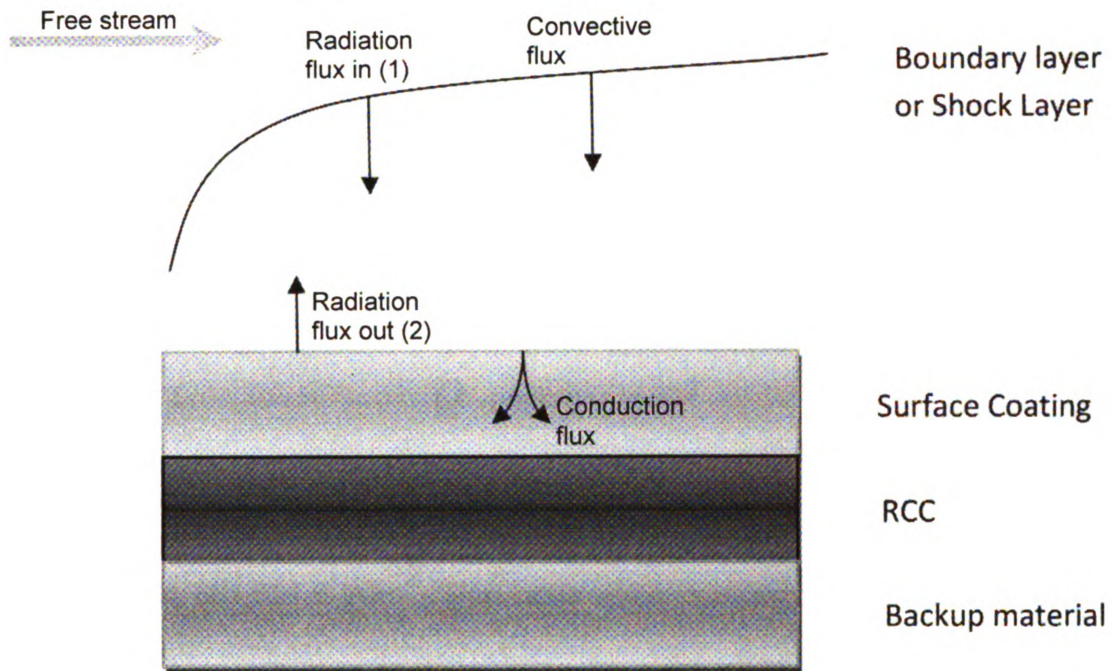
Figure 14. Major heat flux consideration during re-entry [14]

With the three assumptions mentioned above, the remaining heat transfers that are left to be considered in Figure 14 are the convective flux and the radiation flux out. According to [13, 15, 16], these two heat fluxes have to be at equilibrium, which implies that the convective flux in must be balanced by the radiation flux out. As a result, the convective heat flux that is exerted on the surface of the space shuttle can be calculated by the radiation formula shown in Equation (1).

$$Q = \varepsilon \times \sigma \times T^4 \tag{1}$$

In Equation (1):

Q is the heat flux emitted from the surface, unit: W/m^2

ε is the emissivity of the surface

σ is the Stefan-Boltzmann constant, $\sigma = 5.67 \times 10^{-8}\ \text{W}\cdot\text{m}^{-2}\text{K}^{-4}$

T is the surface temperature, which is in Kelvin scale

From the first assumption, the maximum local heating temperature on the surface of the space shuttle is approximately 1,650 °C. Together with the emissivity of the wall that is around 0.85, the total radiation heat flux is

$$Q = 666{,}000\ \text{W/m}^2 \qquad (2)$$

The highest peak heating reported by the NASA [17] was 60 $\text{Btu/ft}^2\text{/s}$. This is equivalent to 681,391.6 W/m^2. This value when compared to the approximated radiation flux has about 2.26% error; therefore, the approximation found using Equation (1) is fairly accurate.

According to the same report [17], the theoretical model actually predicted that less than 5% of the heat is really absorbed and transferred by the wall into the vehicle. Taking this prediction into account, the actual local heat flux that goes through the wall is approximately

$$Q \approx 33{,}300\ \text{W/m}^2 \qquad (3)$$

For the convenience of finite element simulation, the heat flux is taken to be 30,000 W/m^2.

CHAPTER 2

RESULTS FROM PREVIOUS STAGE

DESIGN CONCEPT

After knowing the limitation and the structure of the current TPS and RCC, it is important to develop a new self-cooling system that can enhance the durability and reliability of the space shuttle. In the beginning stage of this project "Perspirable Skin", Sun and Oguz [5, 18] proposed the design of the perspirable skin to be a multifunctional material system, which is arranged in a "peg and hole" fashion.
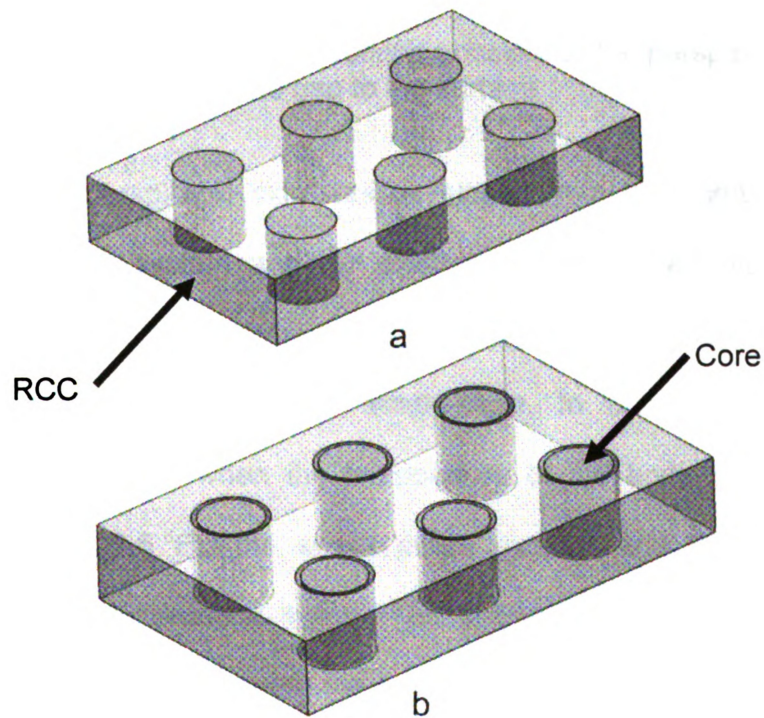
Figure 15. Schematic drawing of the fundamental design concept. (a) When the skin is closed at room temperature; (b) opened at working temperature [5]

The cores in the perspirable skin would be in contact with the RCC under normal room temperature and conditions. During a re-entry, when the surface is heated up to a high temperature, the cores with negative CTE would shrink in order to create small gaps which are sufficient to allow coolant gas to pass through to the surface of the space shuttle.
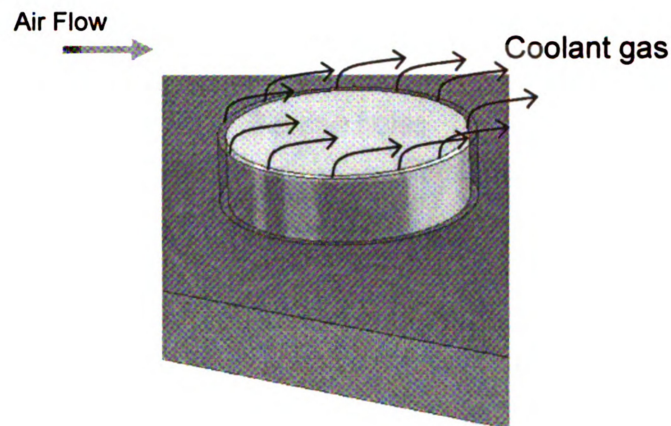
Figure 16. Conceptual idea of the working principle of the perspirable skin when coolant gas is blown through the gap to the surface

The idea of the perspirable skin was developed from the combination of the human perspiration system and the existing cooling system applied to high temperature turbine blades. In the human body, perspiration is the most effective method for regulating the body's temperature. In human skin, there are numerous sweat pores; when the temperature of the body gets higher than normal 37.0 °C (98.6 °F), the sweat pores expand and the sweat glands underneath the skin produce sweat. The sweat is mainly water and some minerals. As it is evaporated from the surface of the skin, heat is removed from the skin and, thus, the body is cooled down.

This natural phenomenon is also adapted in a high temperature turbine blade cooling system. In advanced gas turbine blades, repeated rib turbulence promoters are built into each blade through which compressed cooling air flows. The compressed cooling air is ejected to the surface of the blade through tiny holes and slots. The cooling air forms a thin film that cools and protects the blade from the heat [19].
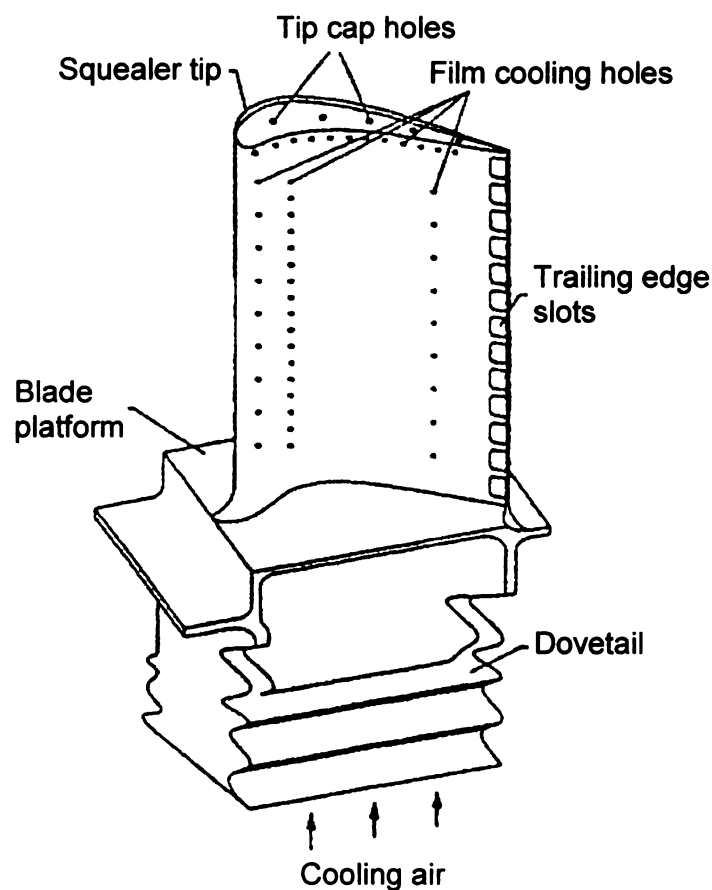
Figure 17. High temperature turbine blade [19]

Such a cooling system has proven to be very effective in advanced high temperature gas turbine blades; nonetheless, it cannot be applied directly to the

space shuttle. Surfaces of the space shuttle orbiter would have to endure extreme temperatures, high pressures during re-entry, and a vacuum while orbiting in deep space. Thus, holes for cooling gas flow must be able to open and close, in response to the temperature and condition changes, like sweat pores in human skin.

The highest working temperature for the perspirable skin is estimated to be around 750 °C to 780 °C because the compound ZrW_2O_8 would dissociate at around 777 °C [5].
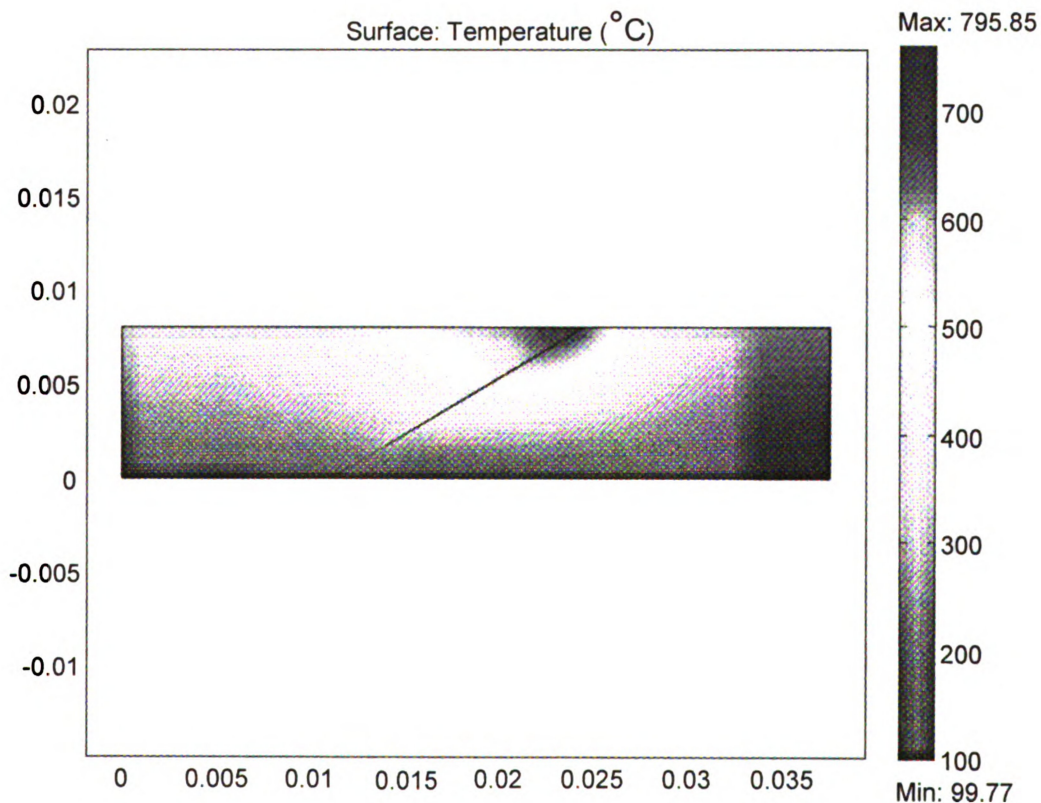
Figure 18. Simulation model with ZrW_2O_8 (top surface: 30,000 W/m^2; bottom surface: 100 °C)

In a simulation performed with ZrW_2O_8, the upper boundary condition was set to have a heat flux of 30,000 W/m^2 applied to the surface; the bottom boundary condition was set with a constant temperature of 100 °C. The result gave a promising prediction, which agreed to the estimations made.

FUNCTIONALLY GRADED MATERIAL (FGM)

Functionally graded material (FGM) is a composite material that is characterized by its gradual change in the composition over its volume. As the composition changes gradually, functionally graded material is non-homogeneous and all the material properties vary with the location in the material. Figure 20 illustrates the difference between a homogeneous material and a FGM.

Homogeneous material   Functionally graded material
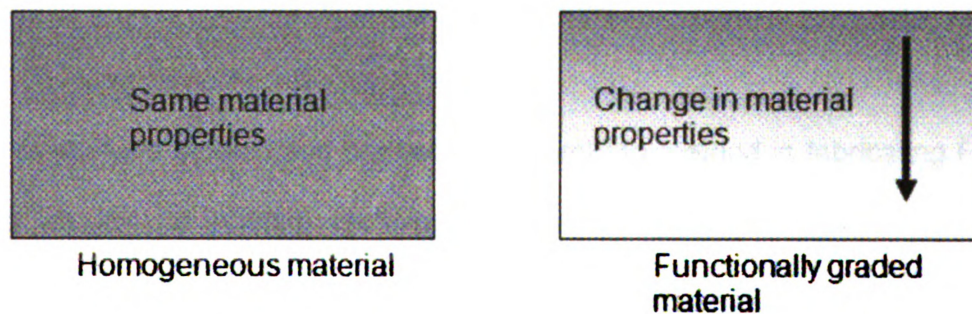
Figure 19. Illustration of functionally graded material

In the laboratory, most of the effort has been focused on manufacturing FGM from zirconia (ZrO_2) and aluminum oxide (Al_2O_3) [20], as well as ZrW_2O_8 from ZrO_2 and tungstate (WO_3) [21]. ZrW_2O_8 has been chosen to be the primary

material for the core design because it exhibits a negative coefficient of thermal expansion, i.e., it shrinks when it is heated up. This special feature is really suitable for the application in the perspirable skin design.

There are several different ways to produce FGM proposed by researchers around the globe. Lambros et al. have developed FGMs using ultraviolet (UV) irradiation, in conjunction with Poly(ethylene co-carbon monoxide) (ECO), which is a material that degrades rapidly under UV light [22]. Pei et al. explored the fabrication technique utilizing laser beam to melt the alloy substrates, together with additive metals to form FGMs [23]. The mentioned techniques have drawbacks in which the materials have specific properties; such as materials reactive to UV light. Such limitations have prohibited the application of these methods to the fabrication of the perspirable skin, as the ZrO_2 and WO_3 powders are rather inert and do not exhibit such properties.

Mott et al. have studied and opened one promising method in fabricating FGMs, using an ink jet printing technique. The technique is similar to 3D rapid prototyping which the powders used in the experiment were ZrO_2 and Al_2O_3. The printer ejected "inks" were made of ZrO_2 and Al_2O_3 solutions [24]. This technique has revealed the possibility of fabrication FGMs with multi-dimensional gradients in a controlled and simple setup, despite the fact a one-dimensional FMG was fabricated for the research work.

The FGM that is fabricated in the laboratory is a one-dimensional FGM, where the material properties would vary along the thickness of the material only. After a study to examine the many different fabrication methods for FGMs, the powder compaction technique is chosen to fabricate the core for the perspirable skin. Details of the technique will be discussed in the next section.

POWDER COMPACTION

Powder compaction is chosen to be the fabrication method for the perspirable skin for several reasons. This method is commonly used in industries that deal with ceramic, metal, or pharmaceutical powders because of its simplicity and accuracy. Powders are first compacted using die and punch, and then a sintering process may be needed to form the final products. The final products normally achieve the desired dimensions. Powder compaction would also be an economic method as little or no machining is required after the final products are fabricated.

The powder compaction consists of 3 major steps: preparing and mixing the powders, compressing the powder to the desired shape, and sintering the compacted samples. The first step involves preparing the powders by breaking agglomerates into smaller, fine particles in a mixing tumbler with mixing beads. This process ensures that the powder particles loosely flow during the compaction in the following steps. Once the powder is fully crushed into fine particles, correct proportion and an amount of different powders are weighed and

mixed together (refer to Table 3). This process is important as the composition of the powders would control the material and thermal properties of the final product.

In order to produce ZrW_2O_8, the ZrO_2 and WO_3 powders are mixed in the stoichiometric ratio of 1:2 (mass ratio is m_{WO3}: m_{ZrO2} =1:0.266) [5]. The other ZrO_2/WO_3 mixtures with other mass ratios are shown in Table 3 below.

Table 3. Different compositions of FGMs

Composition type	WO_3/ZrO_2 mass ratio in reactant powder	ZrW_2O_8/ZrO_2 volume ratios in the sintered sample	Final relative density
1	0.159:1	20:80	77%
2	0.264:1	30:70	79%
3	0.38:1	38.9:61.1	80%
4	0.593:1	51.4:48.5	82%
5	1.096:1	70:30	83%
6	2.307:1	90:10	84%

The second step of the process is compressing the well-mixed powders into the desired shapes using the conventional cold, uniaxial compaction. This step involves applying a pressure of 70 MPa to the die and punches, which are made of high grade steel, along the vertical axis. This compacting process is done at room temperature and the green compact is close to the desired dimensions.

The compaction process is illustrated in Figure 18 shown below. The mixed powder is transferred to the die with the bottom punch inserted in it. The top surface is flattened before the insertion of the top punch. This is to ensure that

the top punch would have maximum surface contact with the powder and evenly

distribute the pressure during the compaction.
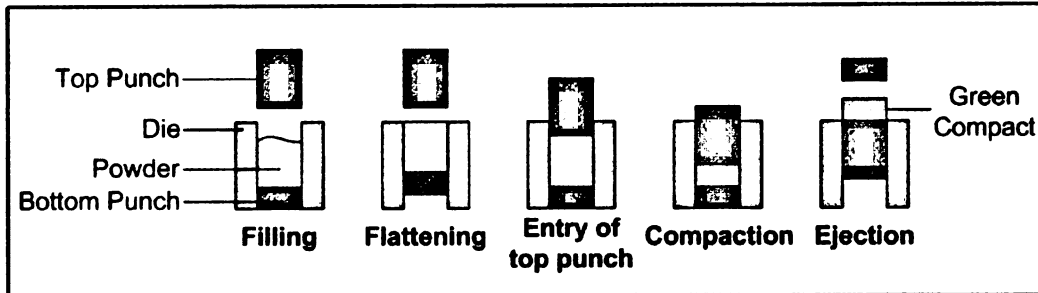
Figure 20. Uniaxial powder compaction

The compaction is achieved by applying 70 MPa on the top punch by a MTS

Instron machine. Lastly, the green compact is ejected from the die from the

bottom and would normally have a density varying from 50% to 70%, depending

on the pressure applied.

Since the green compacts from the compaction process are not fully dense, the

third step of the process, which is sintering, is often essential to produce denser

final products that can reach a density of 95% or higher. Sintering is a thermal

process that bonds the powder particles together at high temperatures by solid-

state atomic transport phenomenon. The green compacts are heated to high

temperatures yet below their respective melting points, and the sintered products

would exhibit a much higher density and strength. The typical sintering curve for

ZrW_2O_8 is shown in Figure 21. The balanced chemical reaction formula for the

process is shown as follows:

$$ZrO_2 + 2WO_3 \rightarrow ZrW_2O_8 \qquad (4)$$
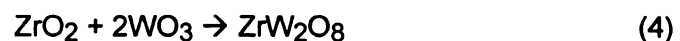
Since the ZrW_2O_8 will decompose at high temperature, the green compact is kept in a platinum crucible during the sintering process. The quenching process at the end of the sintering is to prevent the decomposition of ZrW_2O_8 [18].

After the three processes, the final parts are often functional. However, while the dimensions could just be close to the desired dimensions, sometimes, additional finishing processes might be needed. These processes include machining, grinding, or polishing; these additional processes are essential in order to achieve dimensional accuracy and specific features where powder compaction technique alone cannot achieve.
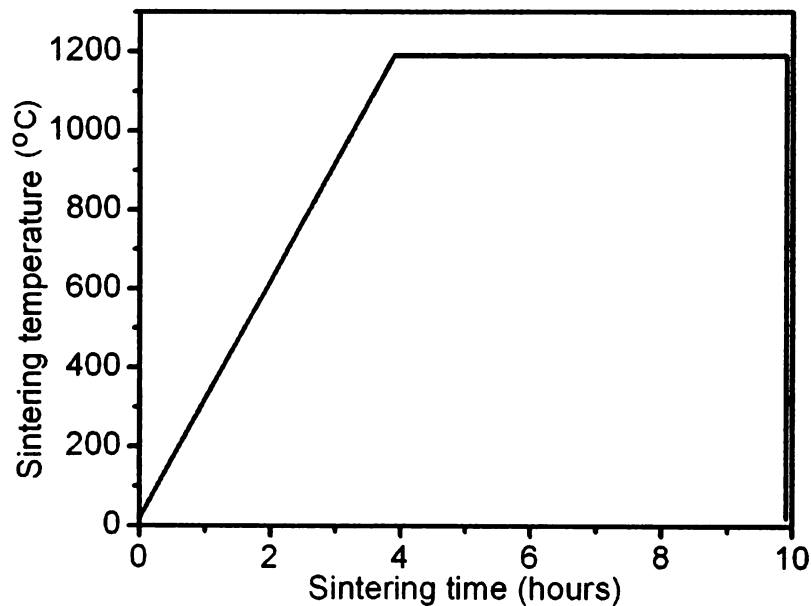
Figure 21. Sintering temperature curve for ZrW_2O_8

CORE DESIGN

Among various fabrication methods and materials, the material that should be chosen for the perspirable skin must meet the extreme conditions. There are several materials that exhibit negative CTE property, Table 4 below shows some of the materials:

Table 4. Negative CTE materials [5]

Material	CTE range (10^{-6} K^{-1})	Temperature range (K)
ThP_2O_7	-9.3 to 4.3	573 - 480
UP_2O_7	-7.1 to 3.1	773 - 1773
ZrV_2O_7	-11.1 to 15.4	380 - 875
ZrW_2O_8	-13.2 to -6.5	3 - 1050
HfW_2O_8	-12.9 to -6.4	3 - 1050

Among these materials, ThP_2O_7, UP_2O_7, and ZrV_2O_7 are not suitable for building the cores for the perspirable skin due to their low CTE ranges; and at higher temperatures they would lose their negative CTE property. In addition, their working temperature ranges do not meet the requirement of a surface material for the space shuttle. Both Hafnium (Hf) and Zirconium (Zr) meet the required working temperature range and exhibit a good negative CTE range. However, Hf is a rare material; and, therefore, Zr would be chosen as the best fabricating material for the perspirable core.

The CTE measurements of ZrW_2O_8 and other varieties of ZrO_2/WO_3 compositions are shown in Figure 22. One very interesting phenomenon

observed is the sudden drop in CTE values for all the compositions except for ZrO$_2$. This huge shrinkage in CTE values occurred at about 150 °C in all the mixtures of ZrO$_2$/WO$_3$ is due to the phase change of WO$_3$. As the amount of WO$_3$ in the mixture increases, the shrinkage would be bigger. If the phase change regions are ignored, the CTE values of these compositions behave as constants for a wide range of temperatures.
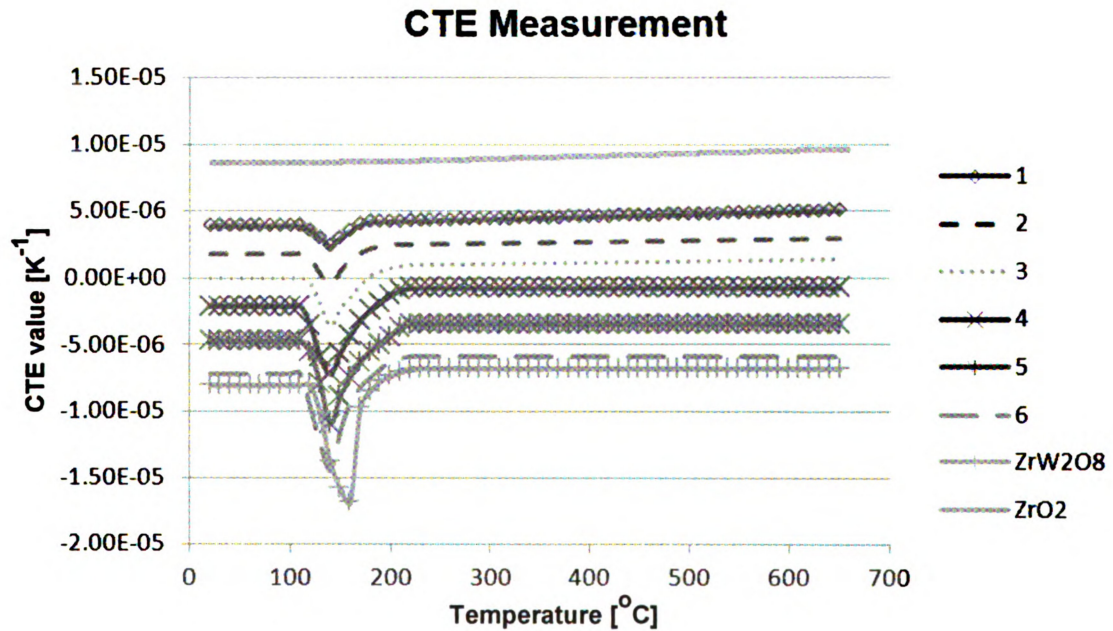
CTE Measurement

Figure 22. CTE measurements of different samples produced in the laboratory (refer to Table 3 for the compositions #1 – 6)

After a series of studies in simulating the core designs in a commercial FEM software ABAQUS, the final geometry of the core design for the perspirable skin took the form shown in Figure 23. The core consisted of 5 layers with their respective properties shown in Table 5. In the simulation, the top layer of the core was exposed to a temperature of 760 °C and the bottom layer was set to a

constant temperature of 100 °C. The top part of the core shrank isotropically in conjunction with the shrinkage in the surrounding RCC, generating a total gap width of approximately 100 µm (100×10^{-6} m).

As the lower part of the cylindrical core was made of composite materials with smaller negative CTE values, the shrinkage that occurred in the bottom was relatively minute when compared to the top. Due to this small shrinkage, the bottom part of the core would remain in contact with the surrounding RCC skin. This design feature enabled the core to attach to the system while opening a gap near the surface. The four semi-annular channels were incorporated into the core to allow coolant gas flow during operation.
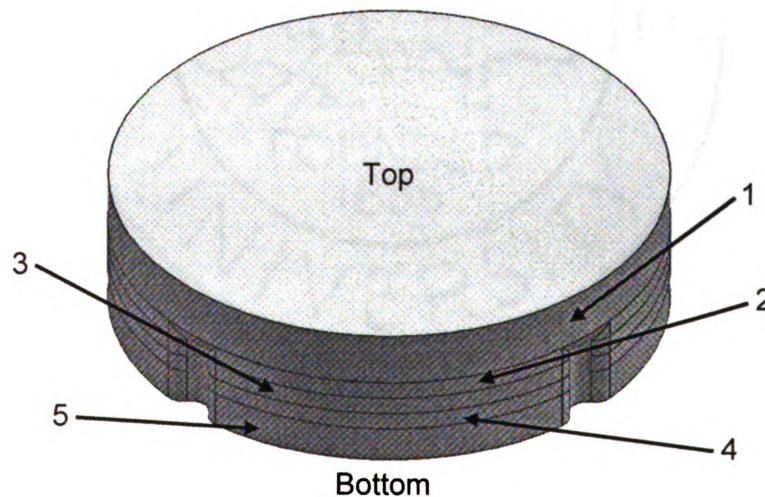
Figure 23. Final design of the FGM core with channels for coolant gas to flow through [5]

Table 5. Design parameters for FGM core

Layer number	ZrW$_2$O$_8$/ZrO$_2$ Volume Ratio	Thermal Conductivity (W/m/K)	Young's Modulus (GPa)	Thickness (mm)
1	100:00	0.9672	4.12 ± 0.13	3
2	88:12	1.0696	3.65 ± 0.13	1
3	76:24	1.1346	3.18 ± 0.10	1
4	64:36	1.2099	2.71 ± 0.08	1
5	52:48	1.4531	2.24 ± 0.08	2

(layer 1: top layer; layer 5: bottom layer)

The ABAQUS simulation shown in Figure 24 represented one quarter of the design because the setup was axis-symmetric. The result illustrated that a gap was formed on the top part surface of the core while remaining in contact with the RCC skin in the bottom part.
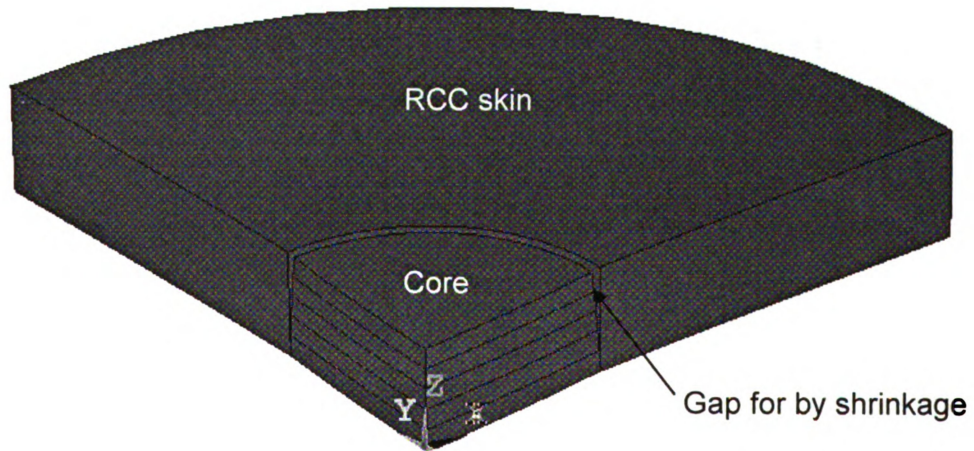
Figure 24. ABAQUS simulation of the perspirable skin [5]

CHAPTER 3

CURRENT STAGE – DEFORMABLE RING DESIGN

NEW CONCEPT

With a proven success in the fabrication and the simulation of the core, this stage of the project aims to enhance the design to increase the gap distance. The new design concept involves the introduction of a deformable ring. The deformation of the ring generates an out-of-plane motion, which is believed to create a bigger opening.
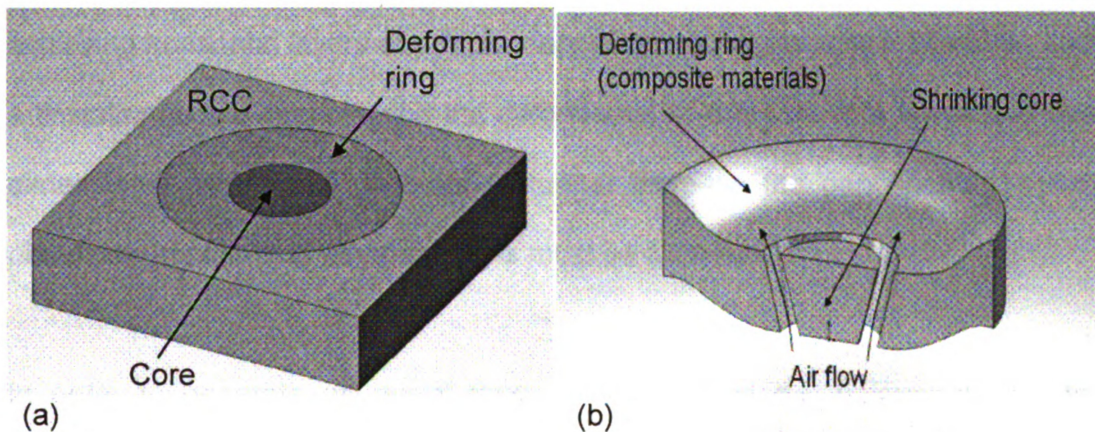
Figure 25. (a) New design concept with the deforming ring; (b) out-of-plane deformation to increase the gap distance

The main focus of this thesis would be to investigate different approaches and combinations to achieve the desired out-of-plane deformation of the deforming ring and the fabrication methods that are suitable for the proposed methods.

With the knowledge of fabricating FMG by powder compaction, the study is conducted to investigate the possibilities of arranging the powders differently within the deforming ring to create a smart material, which produces the desired deformation.

NEW APPROACHES

At the beginning stage of the project, core designs were restricted to flat layers of different composite materials. This was driven by the limitation of the fabrication method because the existing lab equipment and technology are only capable of achieving horizontal layers of powder deposition and compaction. However, such a limitation would circumscribe the deformation of the core to a linear and one-dimensional contraction. In order to further increase the gap opening, out-of-plane deformation and other solutions must be explored.

In order to generate an out-of-plane deformation in the deforming ring, the powder distribution must be irregular and more versatile. The approach to start this new design concept is to divide the cross-section of the deforming ring into fine squares named "pixels". Depending on the amount of shrinkage desired, each pixel would then be assigned a material property based on the CTE value of the material (refer to Table 3). When all the pixels have been assigned a material property, adjacent pixels that have the same material properties would

be coerced to form the same material. A simplified example of the resulting design of the deforming ring is shown in Figure 26.
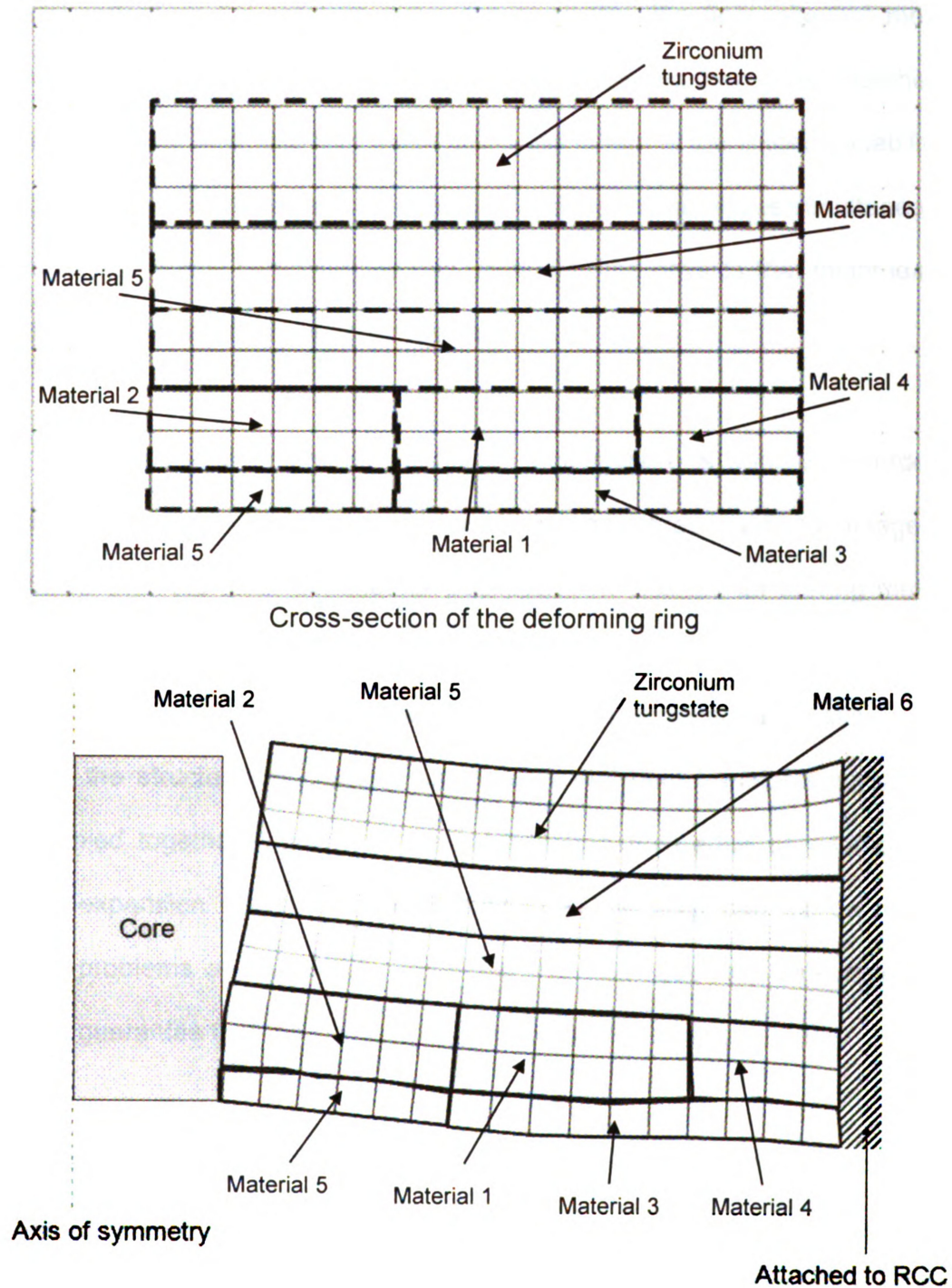

Figure 26. Meshing the deforming ring into pixels

be coerced to form the same material. A simplified example of the resulting design of the deforming ring is shown in Figure 26.
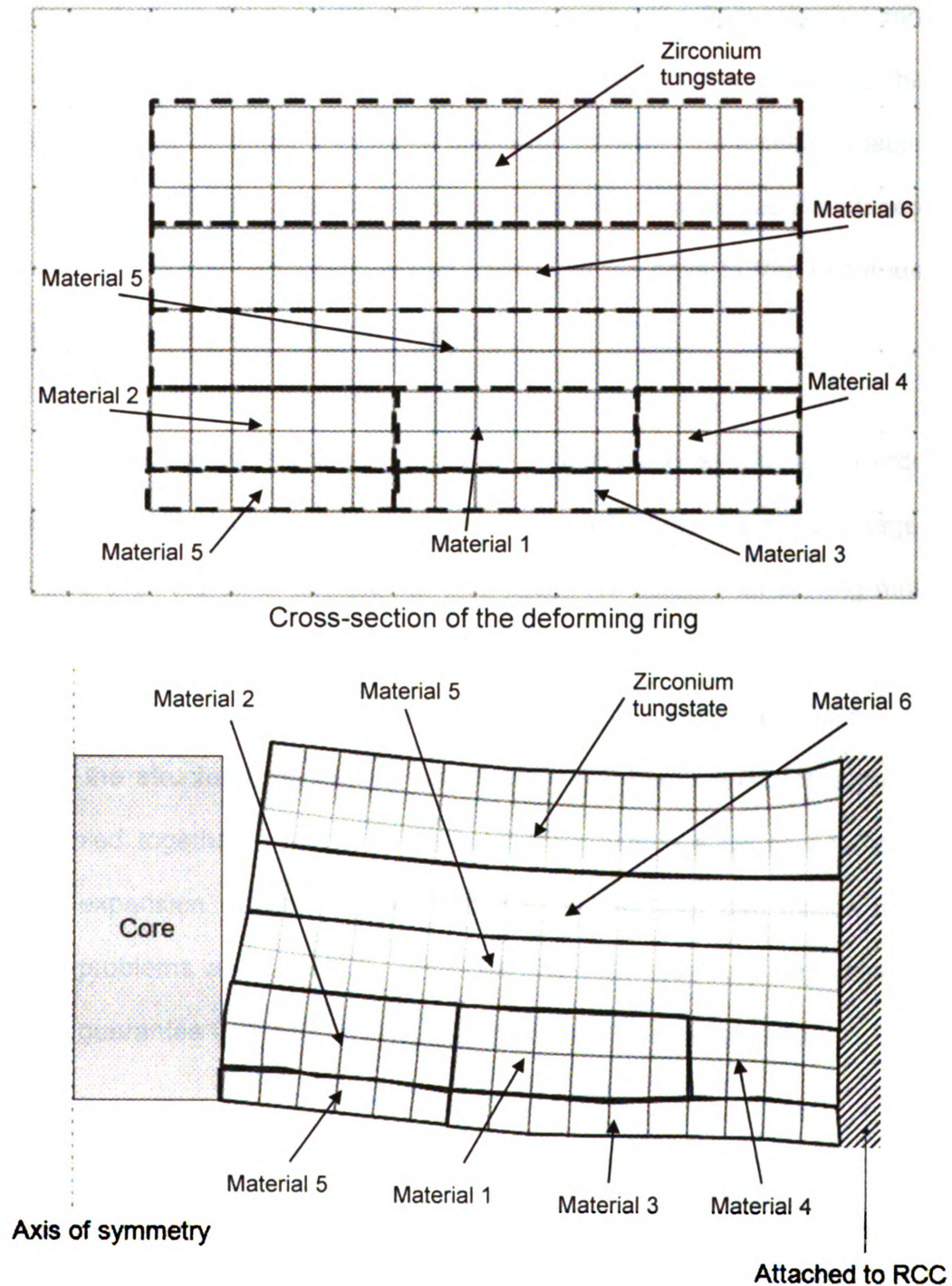
Figure 26. Meshing the deforming ring into pixels

Previously, finite element simulations were done using FEM packages ABAQUS and ANSYS. In order to simulate continuously varying material properties that are dependent on temperature within the geometry, the finite element models were divided into layers with fixed material properties and then glued together as a whole. Another limitation that these packages inherit is the limited capability of computing the coupled physics of structural and thermal analyses simultaneously; therefore, the actual computations had uncoupled the physics that might lead to slight deviations in accuracy of the results.

New FEM commercial software, COMSOL Multiphysics, is adopted in order to accommodate the new concept design. There are three main advantages of COMSOL over the other commercial packages: the abilities for solving multiple coupled physics simultaneously, processing properties that are functions of other variables, and the compatibility with MATLAB. The perspirable skin project involves the structural mechanical and the thermal heat transfer analyses that are coupled together, where the mechanical properties such as coefficient of thermal expansion depend on the temperature. The user can assign multiple physics problems and COMSOL will solve the FEM solutions simultaneously. This will guarantee that the solutions would be realistic and accurate.

The second advantage of COMSOL over other FEM packages ties to its ability to compute multiple physics problems simultaneously. Rather than entering a constant value for properties such as CTE or thermal conductivity the user can

input an equation that is a function of other parameters, such as temperature. Referring to Figure 22, CTE values that are extrapolated from the linear region of each material are entered to COMSOL as a function of temperature (T) shown in Table 6 below.

Table 6. CTE functions for COMSOL simulations

Composite Type	CTE linear curve fit equation (K^{-1})
1	CTE = 2E-09 × T + 4E-06
2	CTE = 1E-09 × T + 2E-06
3	CTE = 1E-09 × T + 8E-07
4	CTE = -1E-23 × T - 8E-07
5	CTE = -1E-22 × T - 3E-06
6	CTE = -2E-22 × T - 6E-06
ZrW_2O_8	CTE = 1E-22 × T - 7E-06
ZrO_2	CTE = 2E-09 × T + 8E-06

As linear as they may seem in Table 6, the CTE values are affected by the high working temperatures, which are as high as over 700 °C. This phenomenon is also valid in other material properties such as Young's Modulus.
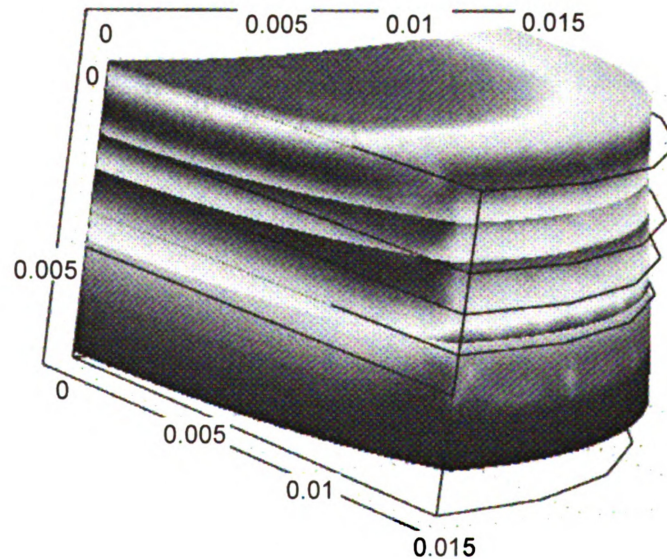
Figure 27. COMSOL simulation of the core design using Table 6 data

COMSOL Multiphysics is tested with the data from Table 6 and verified against the results from previous simulations performed using ABAQUS or ANSYS. Figure 27 shows a quarter of the core design from the previous stage of the project. The gap distance generated by the deformation of the core is compared to previous results and showed a consistency in the displacement. The deformed shaped also matched to the previous work. This verification and validation of the simulation results computed by COMSOL support the migration to this new commercial package.

Last but not least, COMSOL is capable of compiling the CAD and FEM models into MATLAB script files. This feature adds the ability to perform a parametric study to the design process. When the FEM file is converted into the dot-m file (.m extension), which is accessible in MATLAB, parameters can be edited and/or rewritten as variables. This would allow MATLAB to run the simulations varying the values of these parameters to produce the results of a given range of inputs; which minimizes the effort in editing the CAD and FEM files many times in COMSOL.

LAYER PATTERNS

The study of the deforming ring concept took several steps and it is still in the process of exploration and experimentation. With the assistance of COMSOL Multiphysics, the first concept of the deforming ring kicked off with the

composition shown in Figure 26. The initial design is based on the horizontal, rectangular distribution of composite powders for simplicity. The simulation result produced by COMSOL revealed a gap formation at the top surface of the deforming ring; while the bottom was still in contact with the core. This formation of the powder arrangement met the desired deformation, which retained contact with the core at the bottom while opening a larger gap at the top. Figure 28 shows the COMSOL simulation of the cross-section of the deforming ring (the core is omitted in the simulation to reduce computational time).

The drawback of such design is that at least four semi-annular channels must be machined to the bottom of the core as shown in Figure 23. This would add additional complexity to the design and thus increase the production cost of the core due to the machining process. Another drawback with this design is the limited cross-section area of the flow passages.

In order to achieve a better cooling effect, the air flow passage must be widened to increase the volume of coolant gas flowing to the surface of the perspirable skin. The four semi-annular channels could only provide minimal clearance for the gas to flow through. New designs are considered to create greater displacement in the bottom, which would provide feasible solutions to the two mentioned disadvantages of previous core design.
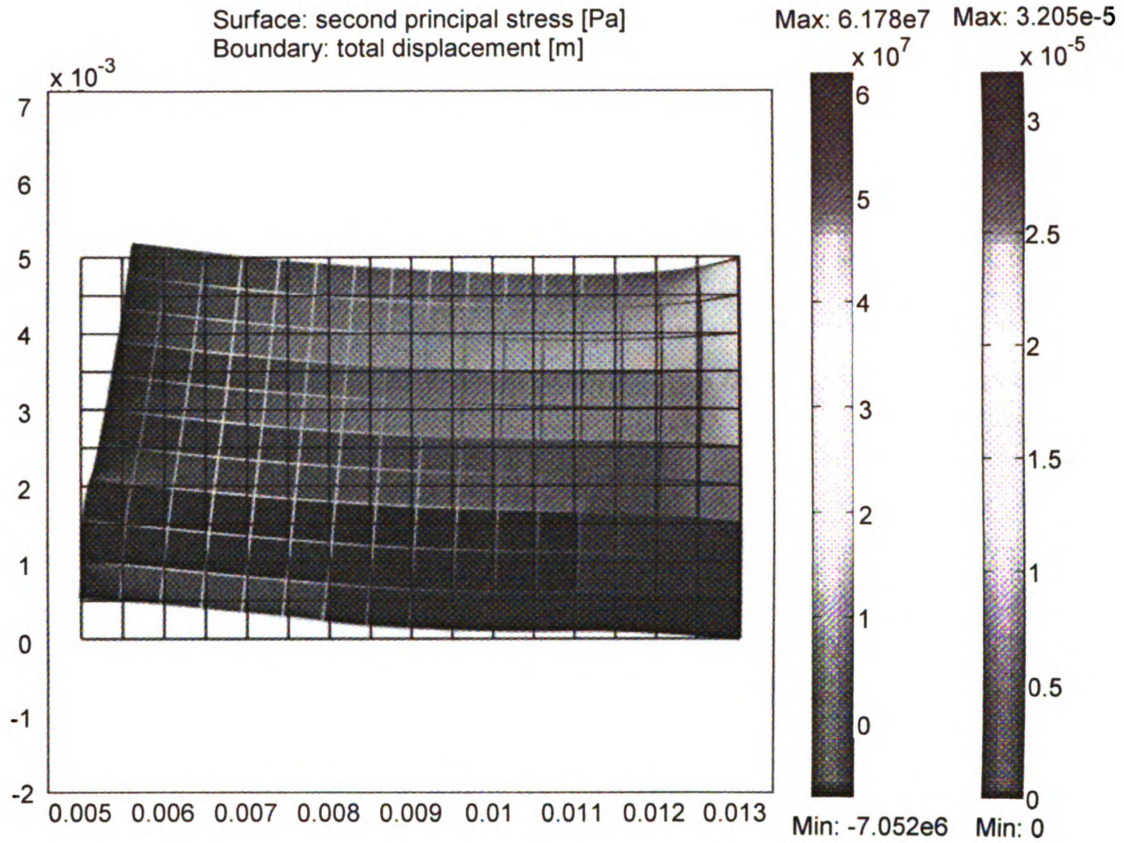
Figure 28. COMSOL simulation of the fundamental design concept of deforming ring

By understanding the shrinkage behavior, the new powder formation is arranged in slant layers as shown in Figure 29. The top and bottom most layers (zone 1 and 4) are assigned with ZrW_2O_8 materials to produce the largest shrinkage. The middle zone 2 and zone 3 are assigned with composite type 6 and type 5 respectively (Table 3). The black lines mark the non-deformed shape in which the core and the deforming ring are in contact. When the design reaches the working temperature, the top surface is exposed to a high temperature of 760 °C while the bottom surface is maintained at 100 °C. This temperature gradient would

cause the top portion of the deforming ring to bend upward (outward deformation if considered in 3-dimensions). This great deformation is achieved by the shrinkage of the large amount of ZrW_2O_8 material in zone 1. The change in materials through zone 2 and 3 help to create a gradual reduction in CTE values, in which the stresses formed between zones are minimized. Despite the lower temperature, zone 4 has used ZrW_2O_8 to create gap formation at the bottom.
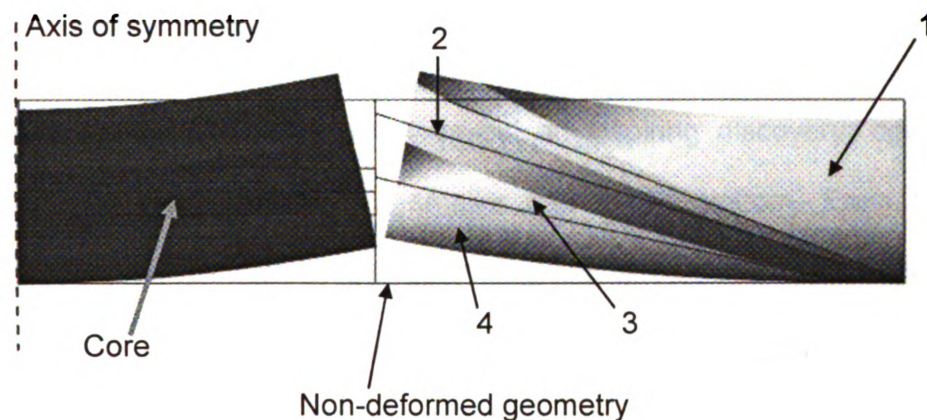
Figure 29. Slant layers design which opens a bottom gap for more coolant gas flow

In order to explore the possibilities to further widen the gaps, the finite element model has been converted into MATLAB script file for parametric study. The aim is to investigate the correlation between the cross-section area of zone 1 and gap distances at the top and the bottom. In Figure 30, the diagrams show the boundary dividing zone 1 and 2 moves in different directions and gradually generates different cross-section areas. The left shows the transformation of zone 1 diminishing and eventually zone 2 takes over; whereas the right illustrates that zone 1 has shrunk to the side wall.
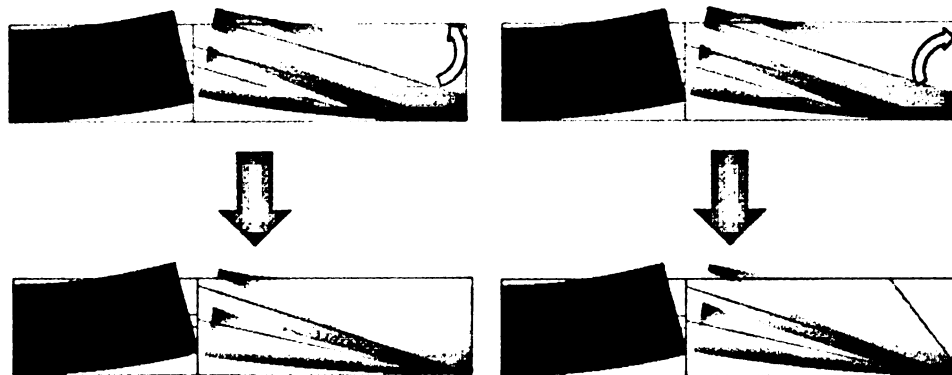
Figure 30. New slant layered design of the deforming ring

The results of the parametric study reveal an inspiring discovery: opening a larger top gap would result in a smaller gap at the bottom. From the left transformation, deformation of the deforming ring is minimal when there is no ZrW_2O_8 material on the top section. As a result, the top gap distance is reduced, but the bottom gap distance is increased with less deflection of the ring. The transformation on the right illustrates that the deformation is increased and thus bringing more displacement at the top gap. However, this has an adversarial effect to the bottom gap, where the gap distance is reduced because of the higher deflection of the deforming ring.

This inverse phenomenon has brought the understanding that solely changing the powder arrangement cannot achieve the desire goal. The geometry of the deforming ring must be re-examined and designed to increase the top gap distance while maintaining a significant clearance at the bottom.

CUT-OUTS

Many other ideas and arrangements of the powder layers have been explored before, but none of these solutions has proven a significant increase to the gap distance both at the top and bottom. The major issue in the design remains: increasing the gap distances while providing significant clearance between the core and deforming ring at the bottom.

To effectively solve the issue of the clearance at the bottom of the opening is achieved by altering the geometry of the deforming ring as shown in Figure 31 below. A wedge is cut off the bottom corner of the deforming ring to eliminate the effect of narrowing the clearance at the bottom when the deforming ring bends upward.
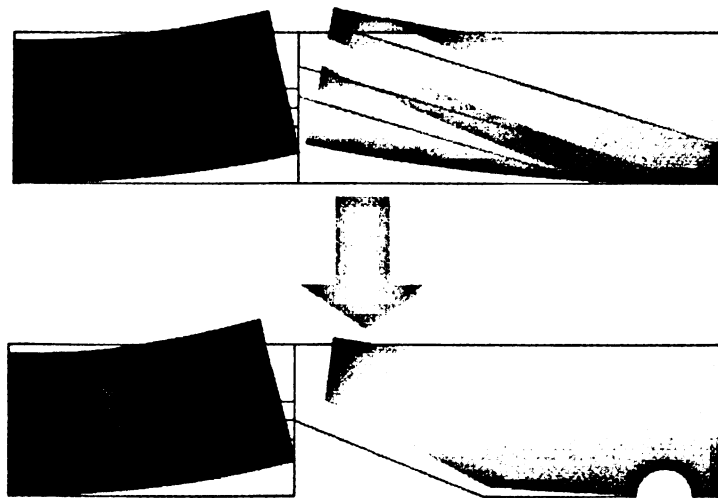
Figure 31. Cut-out design with a wedge to overcome bottom gap issue

This wedged arrangement of the deforming ring, however, does come with a reduction on the overall deformation of the ring; the top gap distance is slightly affected by this proposition. This is a result of the reduction in the amount of negative CTE materials that make up the deforming ring.

To compensate the effect of the wedge cut-off, semi-circular cut-outs are added to the deforming ring geometry as shown in Figure 31. The purpose of incorporating cut-outs is to reduce the strength of the structure by creating higher stress points; these locations will be the weak spots for larger deformation. To determine how many semi-circular cut-outs should be put into the geometry or how large each cut-out should be, four different designs are used to investigate the number of cut-outs required for the geometry; and MATLAB in conjunction with COMSOL are used to perform the analyses.

One cut-out   Two cut-outs

Three cut-outs   Five cut-outs
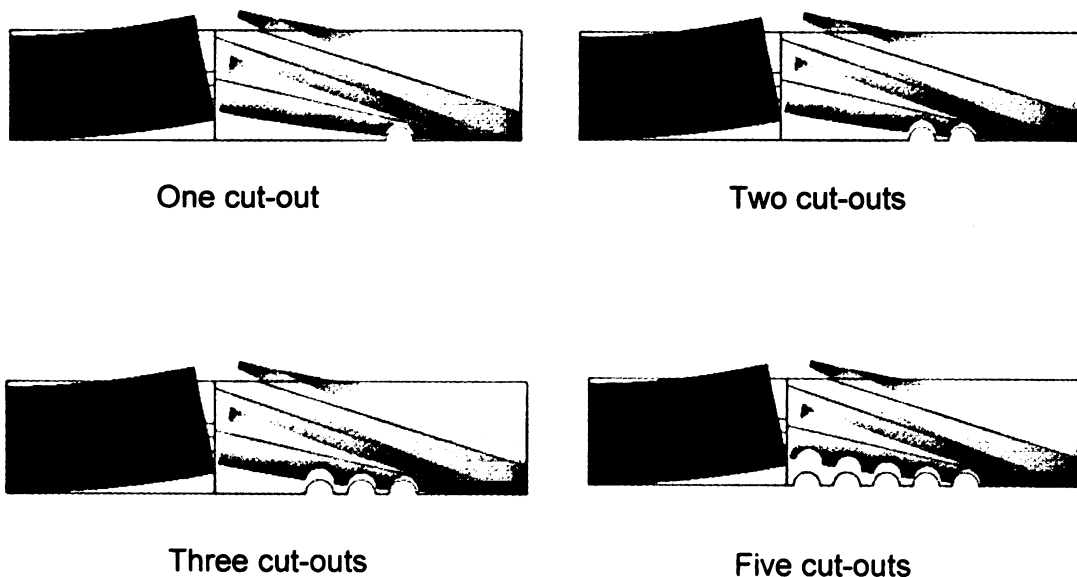
Figure 32. Cut-out designs analyzed

For each of the above designs, a parametric analysis is performed to investigate the relationship between the cut-out radius and the generated gap distances. Coincidently, all the four analyses produce a similar trend in both top and bottom gap distances as shown in Figure 33. It must be emphasized that the bottom gap results shown in Figure 33 and 34 do not include the wedge cut-off design; therefore, the resulting bottom gap distance is minute.
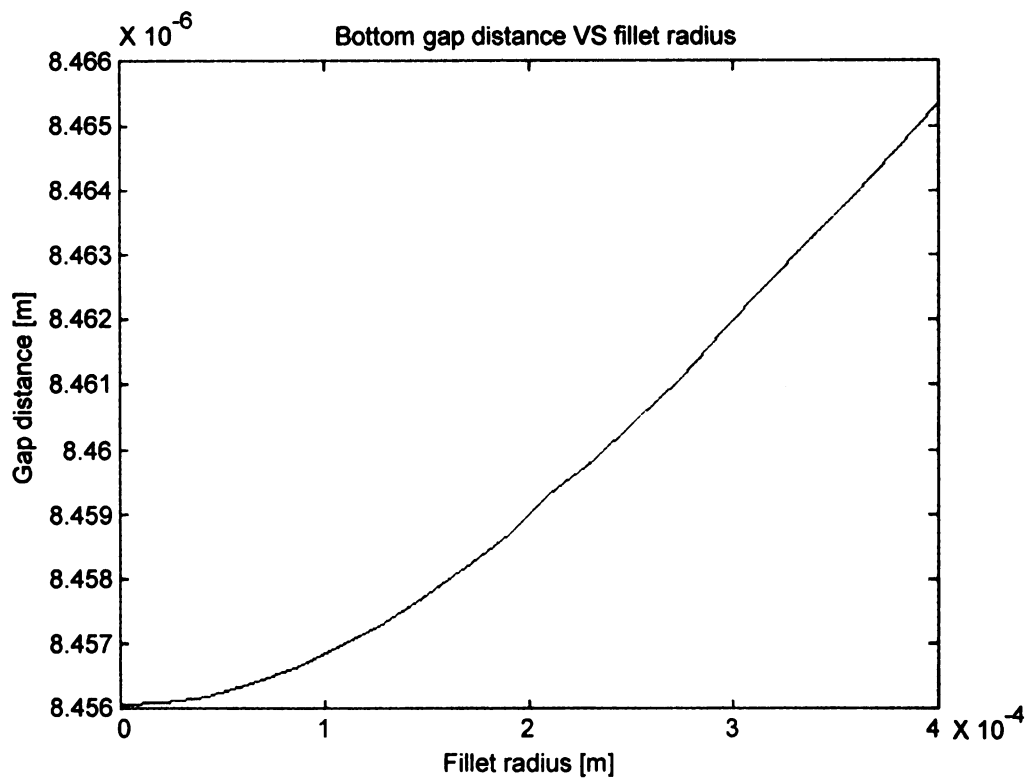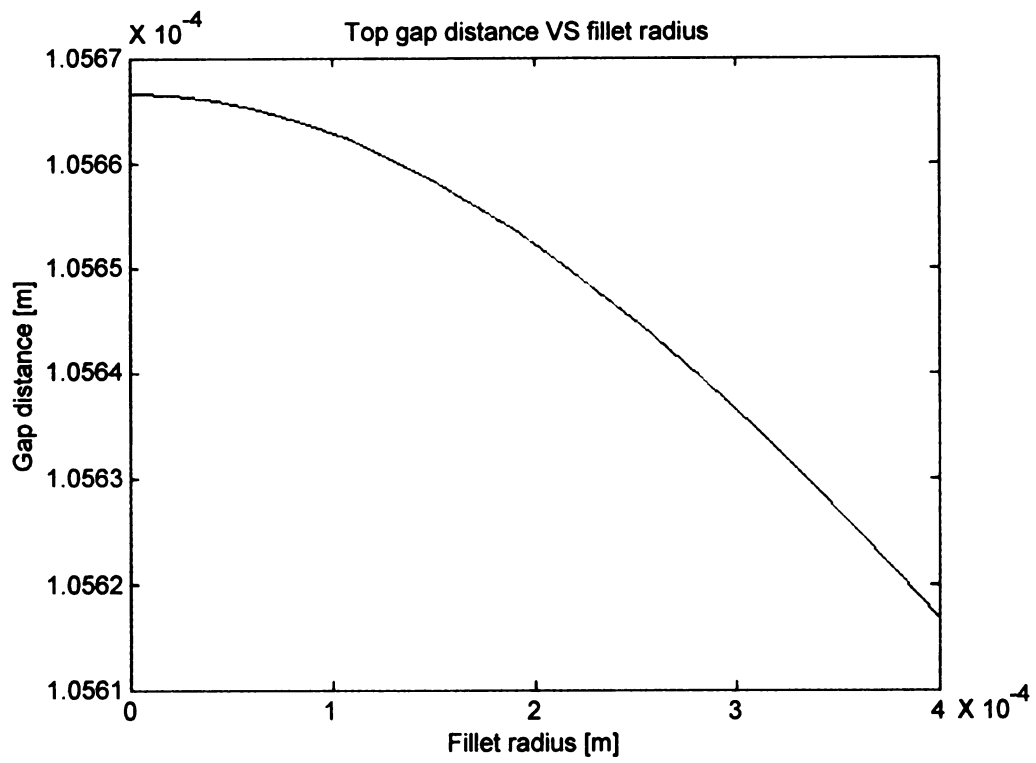
Figure 33. Gap distance analysis for two cut-outs
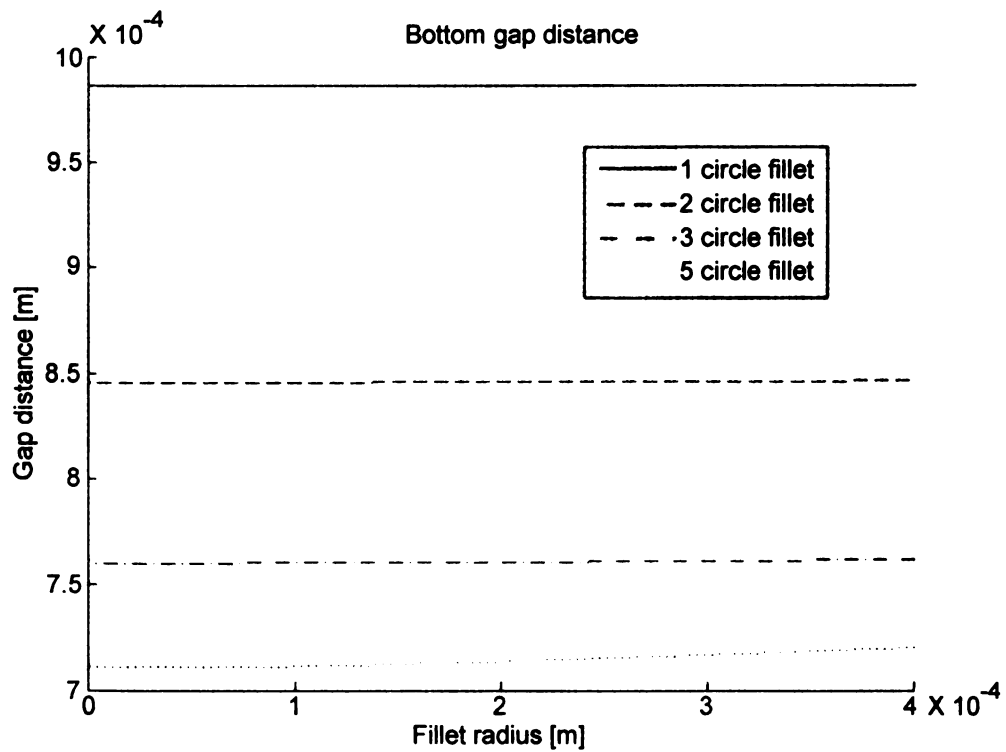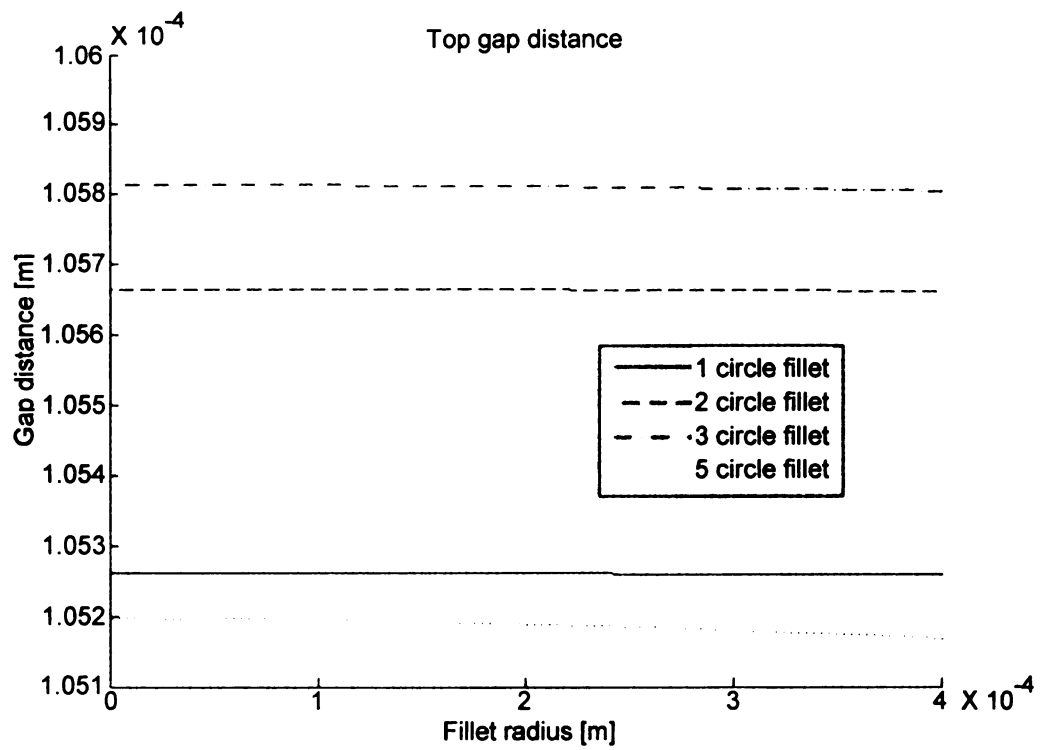
Figure 34. Top and bottom gap distance comparisons for the four cut-outs designs

In Figure 34, the results from the parametric analyses from MATLAB are combined and compared. The top and bottom show the comparisons of the top and bottom gap distances respectively. In the top gap distance comparison, the design with 3 cut-outs achieved the largest distance followed by 2 cut-outs; whereas 1 cut-out and 5 cut-outs designs showed relatively smaller gap distances. The 1 cut-out design on the other hand has the largest gap distance at the bottom gap analysis, followed by 2 cut-outs, 3 cut-outs, and 5 cut-outs in descending order of gap distance.

Despite the fact that 3 cut-outs and 1 cut-out designs have distinctive gap distance in the top and bottom gap analyses respectively, they do not achieve a well overall performance in both cases. On the contrary, the design with 2 cut-outs shows a relatively large gap distances in both top and bottom analyses. This desired overall performance has made 2 cut-outs the most favorable design.

From the analyses, it is noted that more cut-outs such as the design with 5 cut-outs do not necessary prove to be effective. This result can account for the reduction in the materials. As more cut-outs are made to the geometry, more negative CTE materials would be removed; the overall deformation would be reduced. The result of this reduction in deformation is small displacements in both the top and bottom gaps. The previous two analyses have revealed and confirmed that the design with 2 cut-outs has the best performance in generating

great gap distance. Additional analysis is carried out to investigate relationship of the diameter of the cut-outs and the gap distance.
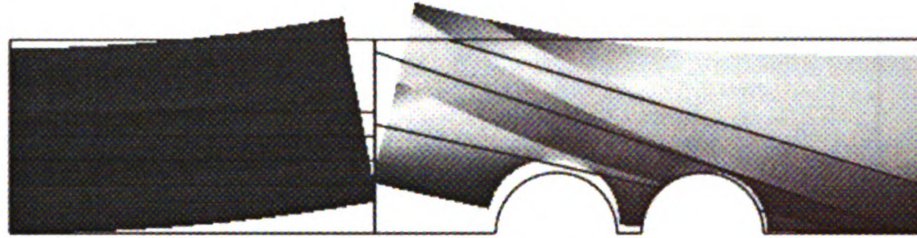
Figure 35. Parametric study on the effect of the diameter has on gap distance

The results of the analysis are shown in Figure 36 and 37; they have revealed that to achieve large openings in top and bottom locations, the optimum diameter of the cut-outs should be 2.5 mm.
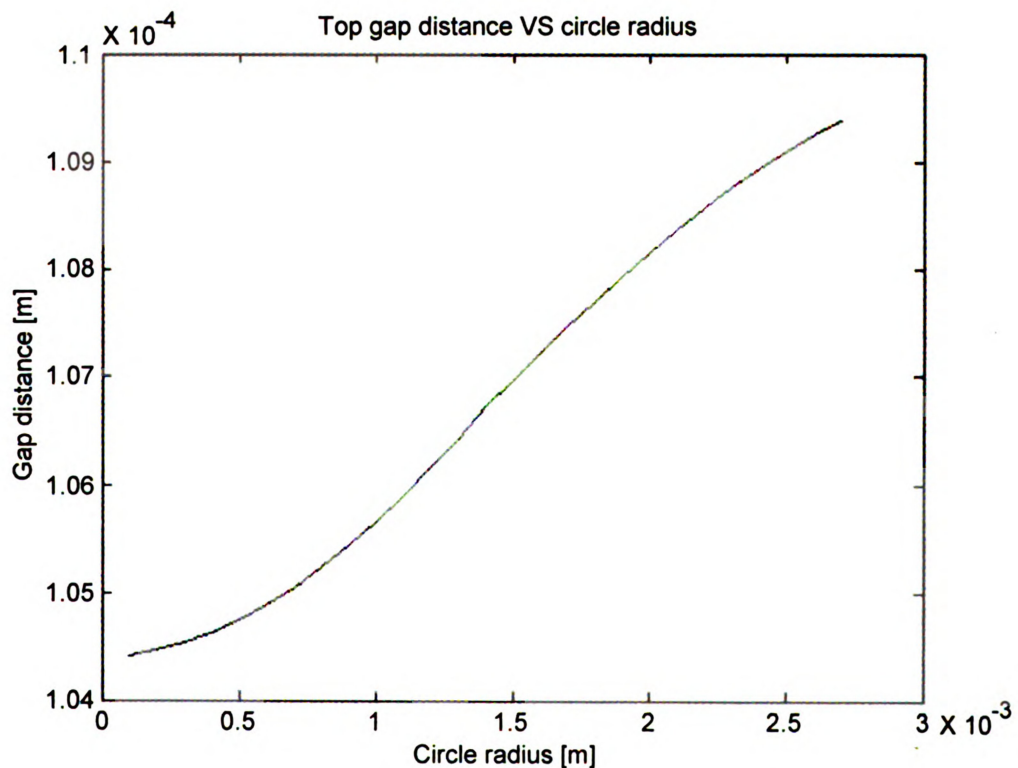
Figure 36. Top gap result of the parametric study
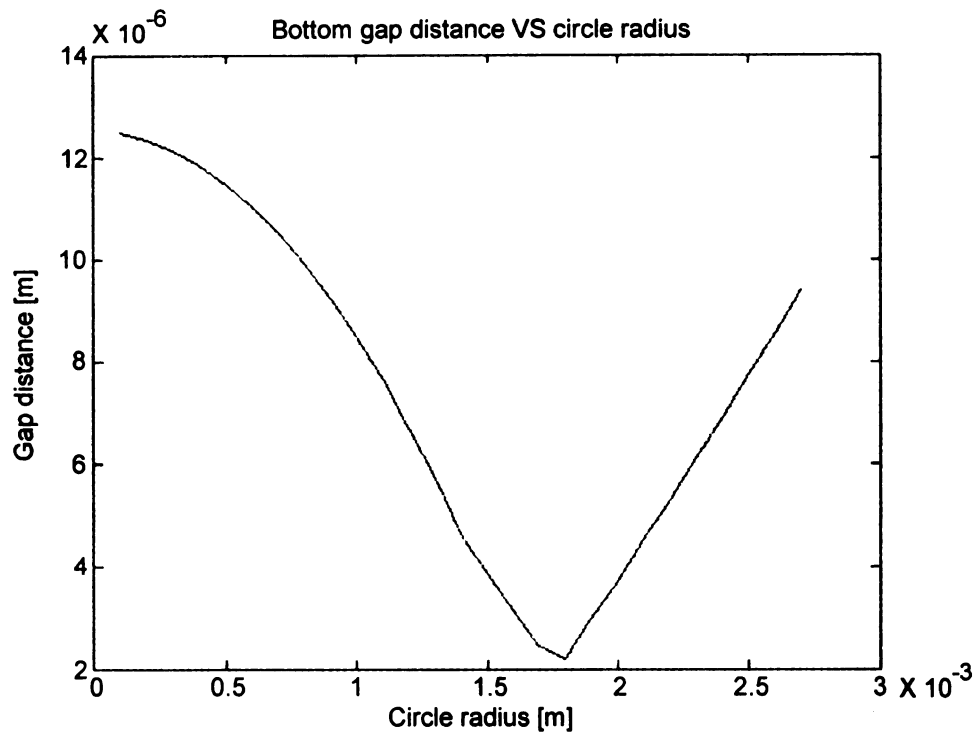
Figure 37. Bottom gap result of the parametric study

MECHANICAL ADVANTAGE MECHANISM

In the previous two sections, two approaches of changing the arrangement of the powder layers and introducing weak spots to facilitate more deformation in the deforming ring have been explored. Regardless of these efforts to create a greater opening to allow coolant gas to flow through, the achievements of the gap distances are not appealing. Up to this point, the design concept remains at utilizing the negative properties of the materials to generate out-of-plane deformation upon temperature rise. However, with the limited amount of

deformation that can be created by the temperature gradient, designs should incorporate other mechanisms to enhance and assist the deformation.

Mechanism is commonly used in a variety of applications; examples of mechanisms include lever, pulleys, gears, and screws. In the following designs, the lever mechanism is deployed to the deforming ring structure. The purpose of applying a mechanism to the structure is because of the benefit that the mechanical advantage brings to the design. Mechanical advantage generally refers to the factor by which the mechanism is capable of multiplying the applied force.

For this application, instead of the applied force being multiplied, the displacement of the deforming ring is multiplied. When the location of the force is applied due to the deformation of the structure (analogous to the "effort point"), displacement would take place; through the principle of mechanical advantage, the displacement at the target site (analogous to the "load") would be multiplied. Figure 38 below illustrates the displacement at the "effort point" got multiplied, creating a greater displacement at the "load".

Table 7. Simulation data of designs with lever mechanism and spring design

Thermal loading condition	Temperature (°C)
Top surface	760
Bottom surface	100

Material type	CTE linear curve fit equation
1 = ZrW_2O_8	y = 1E-22x - 7E-06
2 = ZrO_2	y = 2E-09x + 8E-06
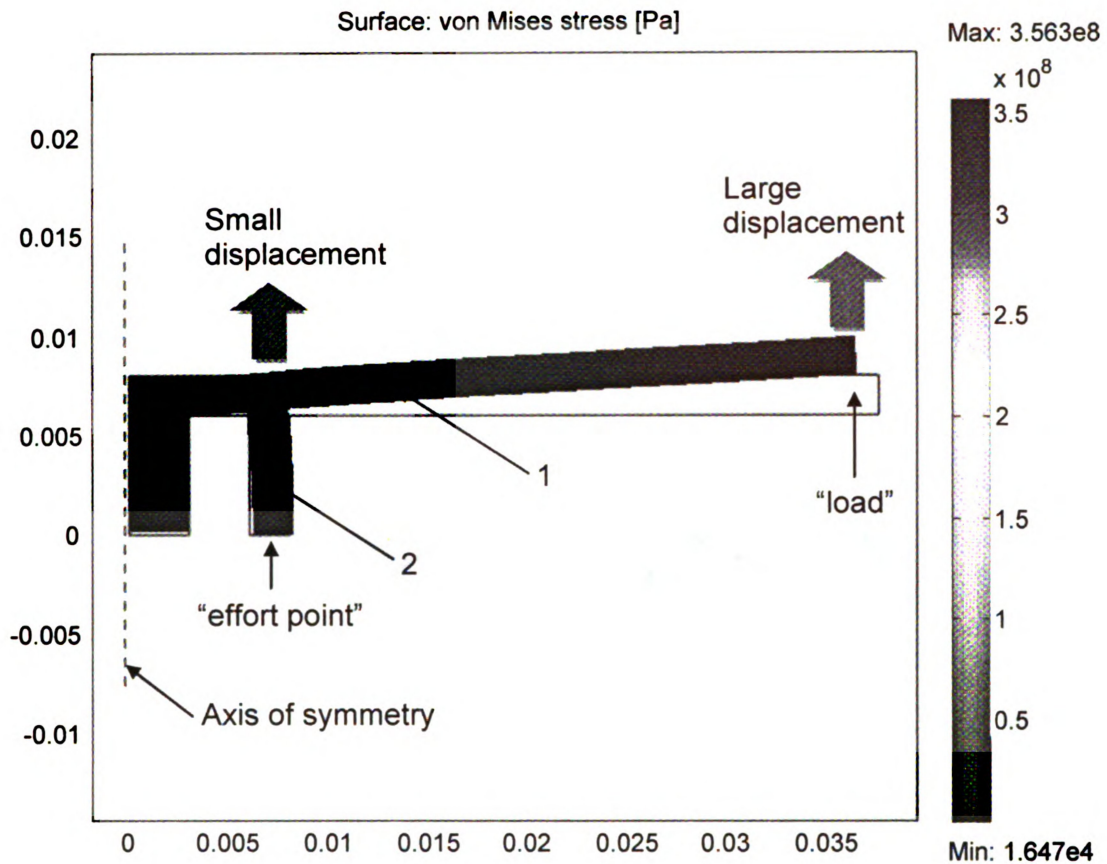
Figure 38. Design with application of lever mechanism

In both designs shown in Figure 38 and 39, it is noticed that the structures marked with type 2 are assigned with pure ZrO_2 material. This material has positive CTE and is needed to generate the necessary expansion for the activation of the lever mechanism. In the alternative design illustrated in Figure 39, the ZrO_2 material is placed at the bottom region where the temperature is maintained at 100 °C. The expansion of the ZrO_2 material is minute since the elevation in temperature is mild; however, this expansion is multiplied and thus creating a huge deformation in the top region. Combining the shrinkage from the

ZrW_2O_8 material making up the top zone, the overall gap distance acquired is larger than the results achieved previously.
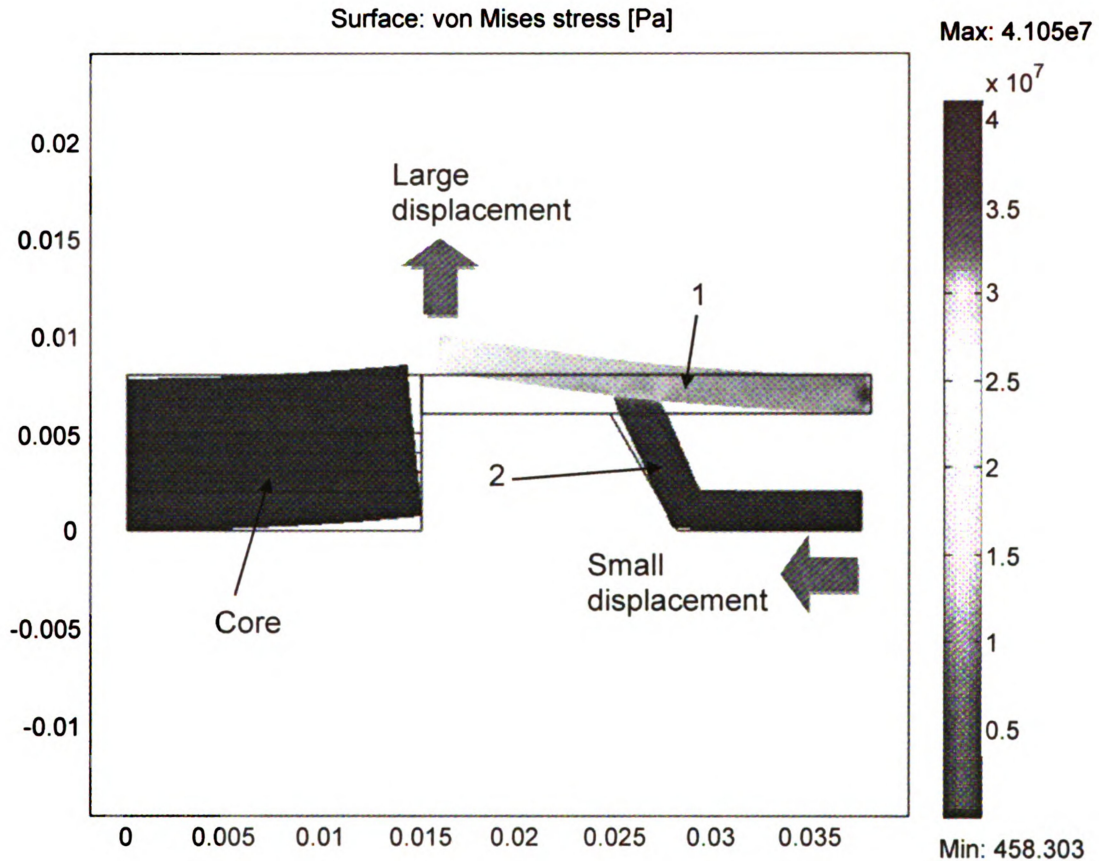
Figure 39. Alternative design using the lever mechanism

The application of mechanical advantage of lever mechanism to assist the deformation brings a larger gap distance to facilitate better coolant gas flow. Nonetheless, the serious shortcoming of this mechanism is the weakened structural configuration, which jeopardizes the integrity of the whole thermal protection system. In the designs shown, they require a large fraction of the structural to be voids; this would lead to a very thin structure of about 2 – 3 mm thick. In addition, high stress points would make the structure of the deforming

ring more fragile and prone to fracture under the extreme working conditions of the space shuttle.

SPRING DESIGN

Parallel to the designs with a mechanical advantage mechanism is the spring design shown in Figure 40. The thermal loading conditions of the simulation and the material properties of the design follow the data used in Table 7, which is shown in the previous section of this chapter.
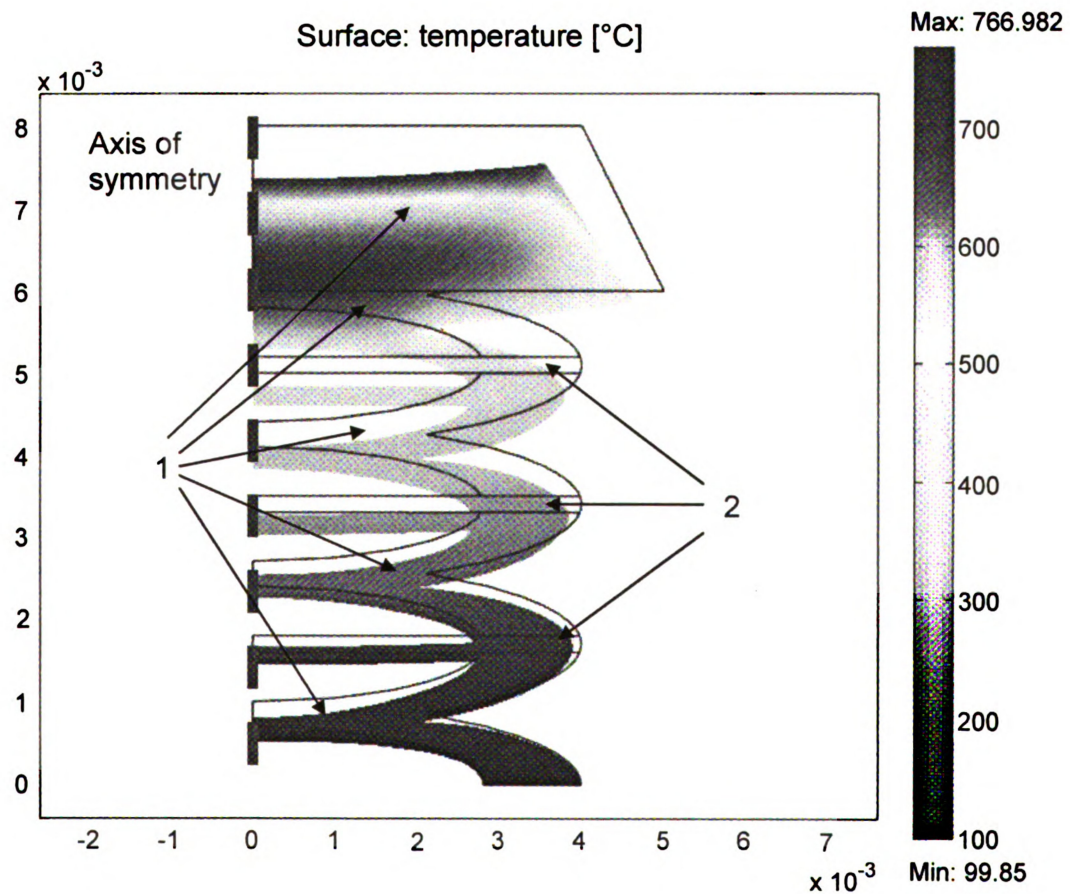
Figure 40. Spring design with wedge top

Different from other design investigated, the spring design does not operate in conjunction with the core. The spring design is developed with the intention to replace the FGM core designed in the preceding stage of the perspirable skin project. The working principle relies on the arrangement of positive and negative CTE materials in alternating sequence. Under the working temperature gradient, positive material would push laterally, while negative material would shrink. This coupling effect would generate a contraction in the vertical direction, thus lowering the top core section downward to open the gap.

Nonetheless, given the complexity of the structure, the spring design has encountered great difficulties in the fabrication. The design comprises voids that are difficult to achieve by powder compaction technology alone. The other unfavorable concern regarding fragility of the structure has also reduced its sustainability.

CHAPTER 4

ALTERNATIVE DESIGN SOLUTIONS

CONCENTRIC RINGS

In the pursuit of the most promising design for the perspirable skin project, many other great ideas have come along and been studied. They began just as conceptual ideas, with the continuous effort from the research group; they were explored and evaluated through FEM and CAD simulations. Although they show strong potentials to becoming plausible solutions to the problem, they pose physical constraints in aspects such as fabrication and actual operation. Perhaps these designs remain theoretical because of current limitations, the advancements technologies and manufacturing might turn the theoretical into practical. The design of concentric rings is one of such proposed conceptual designs.

Inspired by Mayeul de La Tour du Pin who was the exchange student for the research group, he introduced the pioneer idea of concentric rings and cores. The outer ring of the design has a cut-through slot with negative CTE material; the core, on the other hand, has positive CTE materials such as ZrO_2 shrink fitted into the outer ring. The illustration and the properties of the concept are shown in Figure 41 and Table 8 respectively.

As one can notice, the assignments of the materials are in a reversed configuration, the working principle of the concentric ring is different from that of the previous designs. When the design reaches the working temperature (about 760 °C), the inner core would expand according to the nature of the positive CTE materials, such as ZrO_2. Opposite to this deformation, the outer ring, which is made of negative CTE, would shrink and tightly wrap around the core. The resulting gap would be formed at the slot as the expanding core pushes outward against the outer concentric ring.
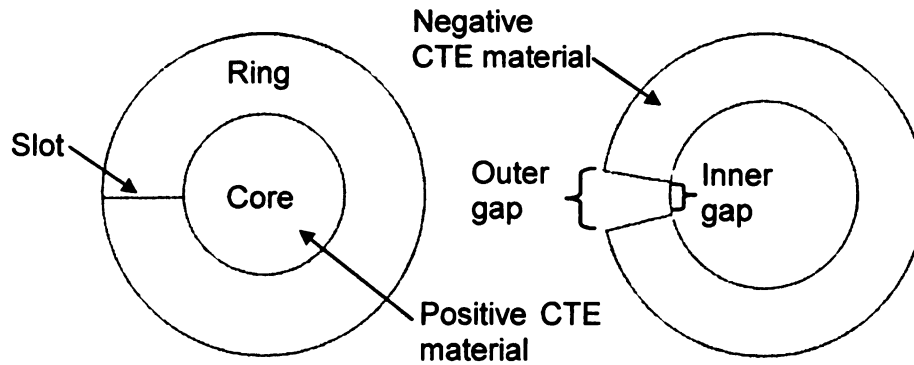
Figure 41. Conceptual design of the concentric ring (left: design at room temperature; right: design at working temperature) [25]

Table 8. Material properties and dimensions for concentric ring design [25]

Part	Radius	Young's Modulus	Poisson's Ratio	CTE
Inner core	7.5 mm	5 GPa	0.3	$7 \times 10^{-6} K^{-1}$
Outer ring	ID: 7.5 mm OD: 15 mm	5 GPa	0.3	$-7 \times 10^{-6} K^{-1}$

Table 9. Concentric ring simulation results [25]

	Design Type	Gap Type	$\Delta T = 600\ °C$	$\Delta T = 800\ °C$
Slot 1		Outer Gap	482 µm	636 µm
		Inner Gap	280 µm	370 µm
Slot 2		Outer Gap	503 µm	626 µm
		Inner Gap	196 µm	260 µm
Slot 3		Outer Gap	466 µm	617 µm
		Inner Gap	232 µm	307 µm
Slot 4		Outer Gap	330 µm	437 µm
		Inner Gap	150 µm	174 µm
Slot 5		Outer Gap	142 µm	282 µm
		Inner Gap	296 µm	386 µm

There are altogether five proposed designs of the concentric ring, each with a slot cut in different orientation and angle. The designs and their respective ANSYS simulation results are shown in Table 9. Two computations are performed at temperature gradients of 600 °C and 800 °C in an effort to

investigate how much the temperature change would have on the simulation results. The average percentage increase in the gap distance is about 36% when the temperature gradient is increased from 600 °C to 800 °C. This study has proved that temperature fluctuation has a predominant influence in the gap distance.

Reviewing all the results, the design with the first type of slot in the concentric ring yields the best overall results in the outer and inner gap distance. Individually, designs with type 2 slot and type 5 slot achieve maximum gap distance in outer and inner gap analyses respectively; however, they do not retain consistency in both temperature gradients. Furthermore, the type 1 slot design has the simplest yet consistent performance in both gap distances over a wide range of temperatures.
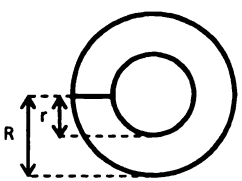
Further parametric study is performed to verify the effect of the size (diameter) of the concentric ring and core on the gap distances, and the results are presented in Table 10. The gap distances vary proportionally with the diameter of the concentric ring and core; the consistency of the increase is observed at both temperature gradients.

Despite the promising results of the simulations, the concentric ring design suffers several major defects that inhibit the advocacy of this design. Regardless of the minute change in the overall dimensions of the design upon heating, the

overall size of the design is expected to increase and thus imposes tremendous stress on the RCC skin around the concentric ring. Knowing that the RCC has nearly zero CTE, the concentric ring and the core would not have sufficient clearance for the heated deformation and is subject to cracking or fracture.

Closely related to the dimensional effect of the design upon heating, concerns have arisen regarding the contact surface between the core and the concentric ring. At working temperature, the core will expand and is tightly embraced by the concentric ring, which shrinks at the same temperature. The huge pressure induced by this shrink fitted configuration creates a lot of friction at the interface where these two components meet. Operation of this gap opening mechanism demands that the concentric ring be able to slide around the core to open the gap at the working temperature. If this motion is obstructed by friction, a fracture might occur at the concentric ring or core, jeopardizing the integrity of the safety of the space shuttle.

Table 10. Diametric comparison of the type 1 slot concentric ring [25]

	ΔT = 600 °C			ΔT = 800 °C		
r / R ratio (mm)	7.5 / 15	10 / 20	15 / 30	7.5 / 15	10 / 20	15 / 30
Outer Gap	482 μm	656 μm	984 μm	636 μm	872 μm	1,308 μm
Inner Gap	280 μm	376 μm	564 μm	370 μm	502 μm	752 μm

SLIDER BAR

The slider bar design is proposed as an alternative that requires further experimentation and simulation to verify its possibilities. From the literature review of the space shuttle, a special metal called Inconel 718 [7] is used in building the ribs of the wings. The properties of this material shown in the Table 11 below and the conceptual idea of the alternative mechanism is illustrated in Figure 42.

Table 11. Material properties of Inconel 718 [5]

Maximum service temperature	980 °C
Approximate melting temperature	1370 °C
Coefficient of thermal expansion (average)	13×10^{-6} m/K
Thermal conductivity	11.4 W/m/K
Density	8,200 kg/m^3

Exterior skin
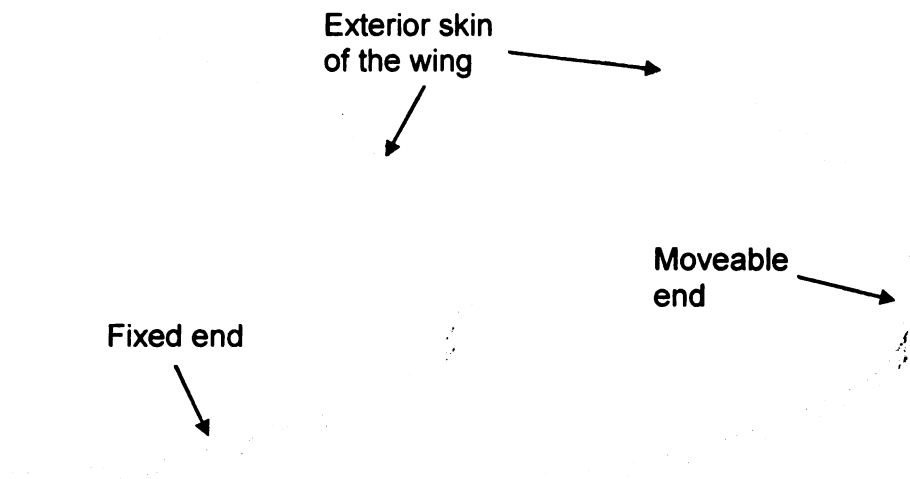of the wing

Moveable
end

Fixed end

Figure 42. Illustration of the slider bar (left: misaligned holes at room temperature; right: the holes align at working temperature) [25]

The working principle of the slider bar simplifies the structural design for composite materials like ZrW_2O_8 and ZrO_2. Figure 42 shows that the Inconel 718 strip is attached to the interior of the skin of the wing. At room temperature, the hole on the Inconel 718 strip and the hole on the exterior skin do not overlap one another, creating a tight seal. When the temperature increases, the expansion of the Inconel 718 strip would extend along the curvature of the skin. The two holes would align and create an opening for the coolant gas to flow through.

The uniquely high service temperature and melting temperature of Inconel 718 open the exploration to different special metals and alloys. Inconel 718's capability of withstanding extreme temperature is the key ingredient to activate this innovative idea. For a simple calculation using the facts of Inconel 718 from Table 11, and Equation (5), a 30 cm long Inconel 718 operating at a temperature gradient of 600 °C would create a gap of size of 2.34 mm.

$$\Delta \ell = \ell \times \Delta T \times CTE \tag{5}$$

SEGMENTED PLATE

Currently, there is a new direction in which the research group is heading for a new opening mechanism for the perspirable skin, the concept of segmented plate design shown in Figure 43. The segmented plate design evolves from the principle of buckling in solid mechanics. Although current manufacturing

techniques and machining equipment may not be able to fabricate this complex geometry, simulations in ABAQUS have shown sustainable results to continue the pursuit in this novel design.
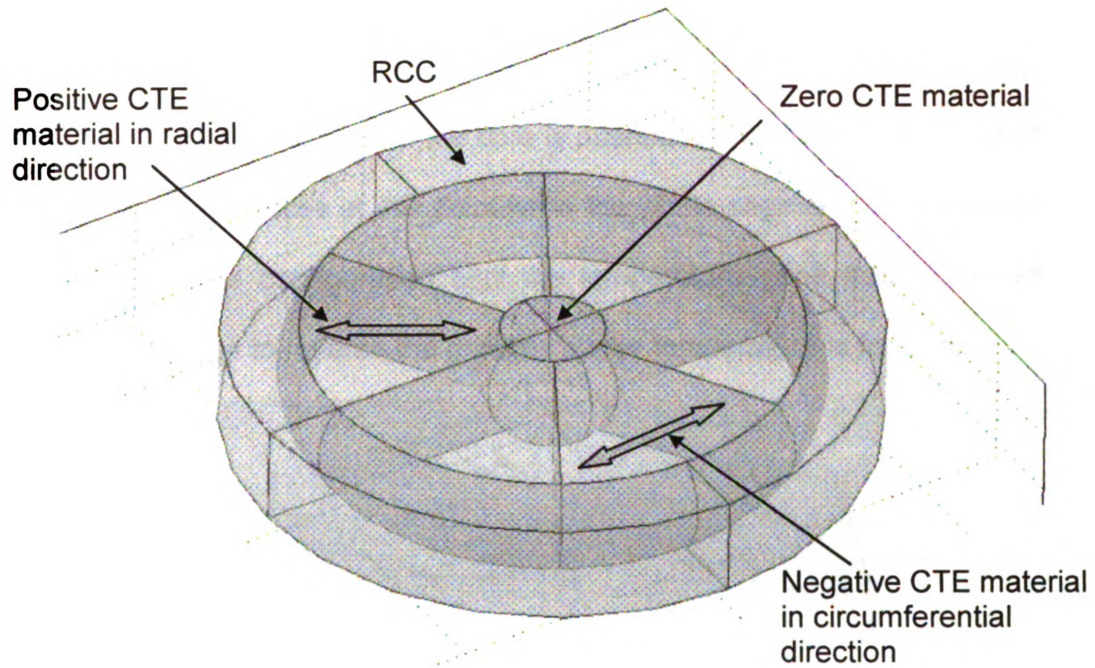
Figure 43. Initial design concept of the segmented plate

At mentioned previously, the working principle of the segmented plate design relies on the buckling effect, which is triggered by the rise in the temperature. One of the difficulties imposed by the design requirement is the multi-dimensional FGM properties of the segmented discs. Indicated by the two different arrows in Figure 43, each segmented disc is made of a multi-dimensional FGM, which has a positive CTE property along the radial direction of the disc. Whereas in the circumferential direction, the material exhibits a negative CTE property. The center core is made of material with a nearly zero CTE material such as the composite type 4 material in Table 6.

As the temperature increases, heat would trigger the segmented discs to expand along the radial direction, but shrinkage occurs in the circumferential direction. While the core remains at its initial size, the discs extend toward the center, compressing the core while creating gaps between adjacent discs. At the working temperature, the expansion of each disc has just achieved sufficient pressure and buckling would occur when the core is pushed downward. Gaps would attain their maximum distances at this point while the whole segmented plate would be maintained at this configuration until the temperature goes down. The whole design is expected to reverse the process as the temperature is reduced.
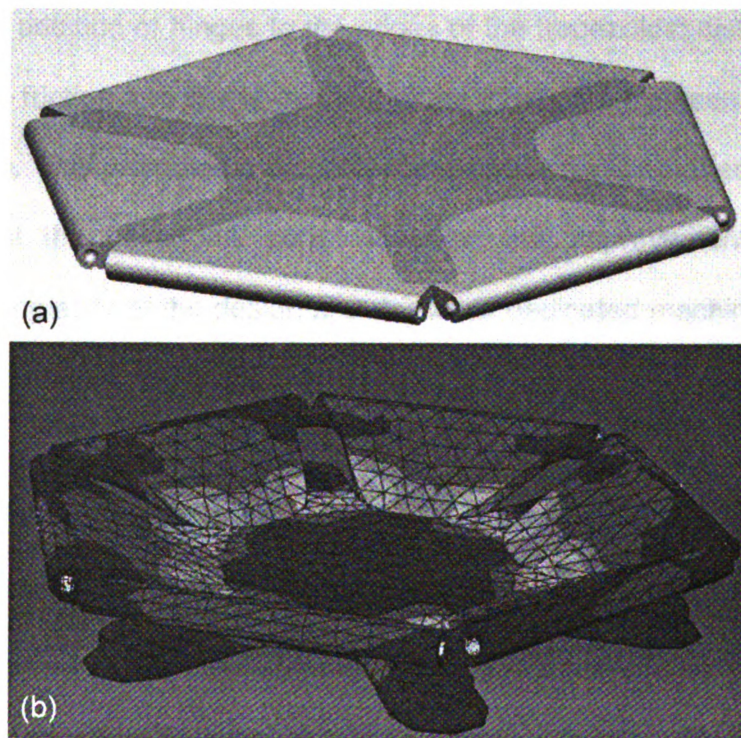

Figure 44. (a) CAD drawing of hexagonal plate by NX; (b) simulation of opening at working temperature using ABAQUS

Using the concept established in the pioneer design, Figure 44 (a) shows a modified model of the segmented plate in a hexagonal configuration. In addition

to the hexagonal shape of the core and 6 trapezoidal discs; hinges are introduced to the edges of the discs to provide greater mobility, as well as easier installation to the RCC skin around the trapezoidal plate. The simulation of the hexagonal plate performed in ABAQUS is shown in Figure 44 (b) at the working temperature. It must be clarified that the simulation does not comprise all the features of a multi-dimensional FGM due to the limitation of the FEM package.

At the preliminary stage of the design, the hexagonal plate has demonstrated a potential solution to open gaps with much larger distances than preceding designs. The addition of hinges to the edges of the trapezoidal discs is expected to reduce the friction and stress induced at the interfaces between the discs and the RCC skin. This promotes a smoother and easier buckling effect as the discs press against the hexagonal core. However, this improvement comes with increased complexity of the design and demands dedicated machining for details such as the chamfers and fillets.

Continuous improvements have been made to perfect the segmented plate design as the research group pursues solutions in this direction. The development of a square segmented plate design is anticipated to further advance the gap distance while aiming to reduce the pressure exerted on the components of the segmented plate. The CAD simulations in Figure 45 demonstrate the working principle of the proposed idea.
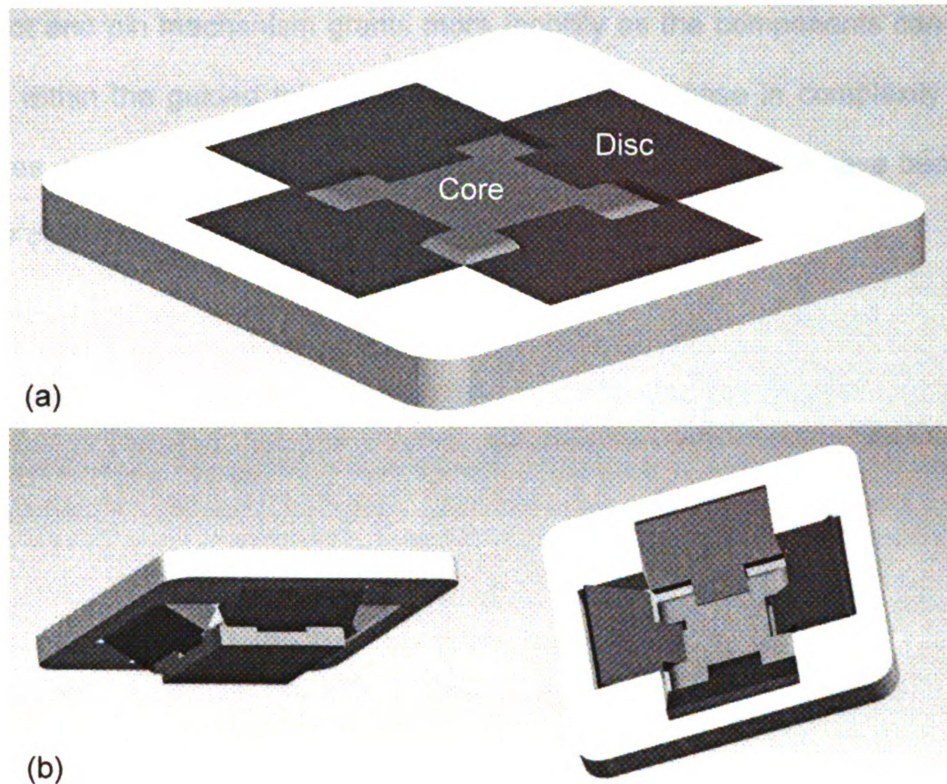
Figure 45. (a) Conceptual design of the square plate; (b) views of the plate opening at working temperature

The new feature to this version of the plate design is the proposed sliding slot and pin mechanism at the connection of the discs and core. Slots are cut into the core where the pins at the protrusions of the discs ride. As the radial expansion of the discs creates a buckling effect, the core would be pushed downward and the pins would slide along the slot to open wide gaps around the corners of the core, simulated in Figure 45 (b).

The slot and pin mechanism is proposed to produce larger openings by the smoothly guided mechanism and to facilitate the recovery of the discs and core back to their respective original positions during cooling down. The advantage of

the slot and pin mechanism grants more mobility as the components can adjust freely within the guided tolerance. Along with the increase in complexity of the features, dedicated machining and tighter dimensional tolerance have become a bigger challenge.

CHAPTER 5

DISCUSSION AND FUTURE WORK

DISCUSSION AND CONCLUSION

Throughout the course of various design considerations and improvements to the perspirable skin, the major properties and behaviors of the FGM deforming ring are observed and documented. The parametric study of the layered patterns and cut-outs of the deforming ring, together with the mechanical advantage mechanism and spring designs, revealed two key features of the ZrW_2O_8 - ZrO_2 composite material: the shrinkage has a dependency on the thickness and the deformed geometry can be determined by the pattern orientation of the layers.

The layer patterns and the cut-out designs proved that the amount of deformation is directly proportional to the thickness (amount) of negative CTE material. If there are more negative materials in the constituents of the design, the deformation achieved by applying the same working temperature is greater than that of a design with fewer amounts of negative materials. From the layer patterns analyses, a greater deformation is a result of putting more negative materials on the top surface where the temperature is higher.

Secondly, intelligently manipulating the patterns and geometry of the deforming ring would control the deformed geometry, as well as the magnitude of

deformation. Stacking different CTE materials in different orientations and layers can achieve a desired deformation; and distinctively introduce voids and/or weak spots to reduce the stiffness can also help to attain better deformation. The four new design concepts have proven that creating higher stress concentration points would assist in the deformation by reducing the stiffness of the structure.

However, it must be noted that excessive removal of material or inappropriate orientation of the powder may jeopardize the overall result of the design. Too many voids and/or higher stress concentration points increase the likelihood of fracture of the deforming ring, which might lead to a catastrophic consequence. Therefore the balance between the magnitude of deformation and the manipulation of the removal of material should be carefully optimized to achieve the best results. In addition, the locations of where these voids and stress concentration points should be introduced would also affect the overall performance of the deforming ring.

At the current stage, incorporating mechanisms such as a lever, spring, and other opening features may face various difficulties in structural design, fabrication, and machining capability. However, the increase in gap distances has been well approved by the simulations, supporting the possibilities to continue exploration in this direction. The ever-changing advancements in technologies and equipment and the designs in virtual space may one day be transformed into reality.

FUTURE WORK

This intermediate stage of the perspirable skin project focuses on exploring different design variations and improvements to perfect the opening mechanism to allow more and better flow of coolant gas of the TPS for the space shuttle. Therefore, much of the effort is put into inspiring, innovative designs and ideas, followed by computer simulations and data analyses of the results. CAD and FEM packages allow a fast and accurate visualization of the concepts and prediction of the designs at operating conditions. Nonetheless, these virtual tools do not reflect real-time and actual performance of these proposed ideas.

Another aspect that has been excluded from the simulations is the effect of the fluid mechanics of the flow of coolant gas has in the overall performance of the design. The exclusion is to confine the project scope to establish the functional geometry of the mechanism of the perspirable skin.

Based on the existing knowledge and findings, together with the placement of new equipment, as the perspirable skin project moves onto the next stage, more experiments can be performed to investigate the hypotheses and simulations. Some of these designs can be fabricated using the powder processing techniques with the current machining capability. The recent installment of the triaxial machine may help to produce geometries like the hexagonal or square segmented plate designs.

During the development of the project, there is a strong need for more understanding and a capability to manipulate multi-dimensional FGMs. Research findings showed that only a small fraction of the science of FGMs had been studied and this remains as a scientific field that is yet to be cultivated. Existing technologies and methods for manufacturing FGMs are limited to some specific types of materials, and often these methods are costly and restricted to laboratory scale. Knowing and gaining the capability to cheaply and accurately produce multi-dimensional FGMs can certainly assist the success of the perspirable skin project.

BIBLIOGRAPHY

[1]   Angelo J. A., 1999, *The dictionary of space technology*, New York, NY: Facts on File, pp. 211-25.

[2]   NASA Facts, 2006, "Orbiter Thermal Protection System", FS-2004-09-014-KSC (Rev. 2006), pp. 1-6.

[3]   Cleland G. G., Iannetti F., 1989, "Thermal protection system of the space shuttle", *NASA contractor report*: NASA CR-4227, pp.1-17

[4]   Richard S., 1980, "Orbiter Protective Tiles Assume Structural Role", *Aviat Week & Spa Tech.*, Feb.25, pp. 22-24.

[5]   Oguz, B., 2009 "Design and processing of perspirable skin through numerical analysis", M.S Thesis at Michigan State University.

[6]   Savage G., 1993, *Carbon-carbon composites*, New York, NY, Chapman & Hall, pp. 37-80 & pp. 322-350.

[7]   Opila E., Jacobson N., and Jerman G., 2004 (Rev. 2006), "Columbia Tragedy. High Temperature Materials Chemistry and Thermodynamic Considerations of the Breached Wing Leading Edge", *Journal of Failure Analysis and Prevention*, pp. 102-110.

[8]   NASA facts, 2006, "Reinforced Carbon-Carbon (RCC) panels", FS-2004-01-001-KSC (Rev. 2006), pp. 1-2.

[9]   Gee S. M., Little J. A., 1991, "Oxidation behavior and protection of carbon/carbon composites", *Journal of Materials Science*, Vol. 26, pp. 1093-1100.

[10]   NASA, 2003, "Working Scenario", *Columbia Accident Investigation Board Report*, Vol. 2.

[11]   NASA, 2003, "Follow the TPS", *Columbia Accident Investigation Board Report*, Vol. 4.

[12]   Ko William L., Fields Roger A. (NASA), 1987, "Thermal Stress Analysis of Space Shuttle Orbiter Subjected to Reentry Aerodynamic Heating", *NASA Technical Memorandum*.

[13] Boulahia B., Belkhiri M., Afrid M., 2008, "Simulation du phénomène de relaxation dans un ecoulement reactif parietal derriere un choc fort", *Revue des Energies Renouvelables*, pp. 890-102.

[14] Laub B., Venkatapathy E. (NASA), 2003, "Thermal Protection System Technology and Facility Needs for Demanding Future Planetary Missions", *International Workshop on Planetary Probe Atmospheric Entry and Descent Trajectory Analysis and Science*.

[15] Fritsche B., Roberts T., Romay M., Ivanov M., Grinberg E., Klinkrad H., 1997, "Spacecraft disintegration during uncontrolled atmospheric re-entry", *Second European Conference on Space Debris*.

[16] Thornton Earl A., 1992, "Thermal Structures: Four Decades of Progress", *Journal of Aircrafts*, Vol. 29, No. 3.

[17] NASA, 2008, "Columbia Crew Survival Investigation Report", p. 2-24.

[18] Sun L., 2009, "Multi-functional materials by powder processing for a thermal protection system with self-cooling capability: Perspirable skin", PhD. Dissertation at Michigan State University.

[19] Han, J. C., Dutta, S., 2001, "Recent Developments in Turbine Blade Internal Cooling," *Heat Transfer in Gas Turbine Systems, ed.*, R. J. Goldstein, Ann. N.Y. Acad. Sci., 934, pp. 162–178.

[20] Sun L., Sneller A., Kwon P., 2008. "Fabrication of Alumina/Zirconia functionally graded material: from optimization of processing parameters to phenomenological constitutive models", *Mater. Sci. Eng. A*, 488(1-2), pp. 31-38.

[21] Sun L., Baldauf S., Kwon P., 2008, "Procession of ZrW_2O_8 –ZrO_2 continuous Functionally graded materials by co-sintering ZrO_2 and ZrO_2+WO_3 multi-layer compacts", *ASME International*.

[22] Lambros, J., Santare, M.H., Li, H., Sapna, G.I., 1999. "A novel technique for the fabrication of laboratory scale functionally graded materials", *Exp. Mech., to appear.*

[23] Pei Y. T., De Hosson J. Th. M., 2000, Acta mater 48(2000), pp. 2617–25.

[24] Mott M., Evans J. R. G., 1999, "Zirconia:alumina functionally graded material made by ceramic ink jet printing", Materials Science and Engineering A271, pp. 344–352.

[25] de La Tour du Pin M., 2010, "Internship report: Design of a perspirable skin", Michigan State University.